bioRxiv preprint doi: https://doi.org/10.1101/2020.06.24.165795; this version posted June 24, 2020. The copyright holder for this preprint (which was not certified by peer review) is the author/funder, who has granted bioRxiv a license to display the preprint in perpetuity. It is made available under aCC-BY-NC-ND 4.0 International license.

Reconstituting Stratified Epithelial Branching Morphogenesis by Engineering Cell Adhesion

Shaohe Wang[1]*, Kazue Matsumoto[1], Kenneth M. Yamada[1]*

[1] Cell Biology Section, National Institute of Dental and Craniofacial Research, National Institutes of Health, Bethesda, MD, USA.

*Correspondence to: shaohe.wang@nih.gov or kenneth.yamada@nih.gov.

Abstract:

During embryogenesis, many organs undergo branching morphogenesis to form tree-like hierarchical structures. However, it remains unclear what drives branching in stratified epithelia, such as in embryonic salivary gland and pancreas. Here, we performed live-organ imaging of mouse embryonic salivary glands at single-cell resolution to reveal branching driven by expansion and folding of an epithelial surface cell sheet characterized by strong cell-matrix adhesion and weak cell-cell adhesion. We successfully reconstituted this early developmental process by experimentally suppressing E-cadherin expression and inducing basement membrane formation in 3D spheroid cultures of engineered cells. Reconstituted branching required integrin-mediated cell-matrix adhesions and was promoted by elevating cell-matrix adhesion strength. Thus, stratified epithelial branching is driven by the combination of strong cell-matrix adhesion and weak cell-cell adhesion of peripheral epithelial cells.

Main Text:

All branching organs have a core epithelium encased by a layer of basement membrane, which is surrounded by a loosely condensed group of mesenchymal cells. Among various roles, the mesenchyme secretes growth factors critical for epithelial growth and morphogenesis (*1–5*). Branching morphogenesis involves extensive dynamics of epithelial cells and the extracellular matrix (*6–8*). Branching epithelia can be single-layered with a lumen or stratified without a lumen, both of which can branch in the absence of mesenchyme when provided with suitable growth factors and extracellular matrix (*9*, *10*). Branching of single-layered lung epithelia involves buckling of the epithelial sheet guided by external sculpting forces from smooth muscle cells that differentiate from adjacent mesenchymal cells (*11–15*). In contrast, the mechanisms used by stratified epithelia to initiate branching morphogenesis remain elusive.

Results

To visualize cellular mechanisms of stratified epithelial branching, we developed live-organ imaging strategies using two-photon microscopy that allowed us to image nearly the entire 3D volume of transgenic mouse (*16*) embryonic salivary glands at high spatiotemporal resolution (**Fig. S1A-B; Movie S1**). Analysis of these movies revealed extensive movement of individual cells throughout the developing gland with the rate of cell movement increasing near the periphery of the branching epithelial buds (*6*, *17*) (**Movie S2**). Next, we evaluated whether cells exchange freely between the outer epithelial layer and gland interior during morphogenesis, or whether branching salivary glands are composed of distinct interior and surface cell populations. To do this, we photoconverted patches of cells near the epithelial surface in transgenic salivary glands expressing KikGR, a photoconvertible fluorescent protein emitting green or red fluorescence before or after conversion (*17*, *18*). Most photoconverted peripheral epithelial cells moved rapidly along the tissue surface while maintaining intimate contact with the basement membrane (**Fig.**

bioRxiv preprint doi: https://doi.org/10.1101/2020.06.24.165795; this version posted June 24, 2020. The copyright holder for this preprint (which was not certified by peer review) is the author/funder, who has granted bioRxiv a license to display the preprint in perpetuity. It is made available under aCC-BY-NC-ND 4.0 International license.

1A; Movie S3), suggesting tight adherence of these cells to the encasing basement membrane. Furthermore, we used an epithelial RFP reporter (Krt14p::RFP) (*19*) that exhibited elevated expression in peripheral versus interior epithelial cells (**Fig. S2A**) to enable automated rendering of the epithelial surface (**Fig. 1B-C; Movie S4**). We analyzed the movements of cells at the epithelial surface (within 15 μm of the gland surface at any point within the tracked time window), which revealed that the movements of most epithelial cells near the surface remain confined to the surface of the developing tissue (**Fig. 1D-E, Fig. S1C-H; Movie S5**). Taken together, we conclude that clefting in stratified salivary gland epithelium is driven by expansion and folding in 3D of a surface cell sheet (**Movie S6**).

Next, we determined whether new surface cells are added uniformly around the epithelial surface or locally at the cleft in order to distinguish between clefting as a systemic or local process. We traced nuclear histone-EGFP intensities of peripheral epithelial cells over time and computed local peripheral curvature to track surface deformation (**Fig. 1F-J, Fig. S2A**). Local expansion to form a cleft predicts an abrupt change of slope angles of temporal nuclear traces at cleft sites (**Fig. S2B**). However, observed changes of slope angles were gradual and surface expansion rates near clefts were indistinguishable from other locations, suggesting that clefting is a systemic activity (**Fig. 1I-J, Fig. S2E-G**). Moreover, increased peripheral nuclear counts over time closely matched expansion of the bud perimeter, indicating constant peripheral cell density (**Fig. 1H, Fig. S2C-D, H**).

We next determined the origin of new epithelial surface cells. The distinct boundary of Krt14p::RFP expression levels between peripheral and interior epithelial cells hinted that new surface cells arise primarily from proliferation of preexisting surface cells (**Movie S6**). However, none of the 289 surface cells whose division was monitored divided within the surface layer to produce two surface daughter cells (Type III; **Fig. 2A**). Instead, 92.4% of the surface cells moved to a subsurface level to complete cell divisions that produced two daughter cells in the gland interior (Type I; **Fig. 2A, Fig. S3A**), and the remaining 7.6% divided in an orientation perpendicular to the surface to generate one surface daughter cell and one interior daughter cell (Type II; **Fig. 2A, Fig. S3B**). Importantly, all surface cell-derived interior daughter cells eventually returned to the surface by reinserting between surface cells, resulting in delayed surface expansion (**Fig. 2B, Fig. S3C-D; Movie S7**). Most cells returned to the surface within 4 hours, but some required >12 hours (**Fig. 2B**). The location of daughter cell reinsertion could be distant from the parental surface cell. In one example, a daughter cell meandered under a forming cleft into a neighboring bud to reach the bottom surface far away from the parental cell location (**Fig. S3E**). Overall, the reinsertion sites were uniformly distributed around the epithelial surface (red dots in **Fig. S3D**), revealing the cellular basis of uniform surface expansion.

What drives the robust surface return of surface-derived cells? Based on the lower E-cadherin expression level of peripheral epithelial cells compared to interior epithelial cells (*20*) (**Fig. 2C-D**), we hypothesized that differential cell-cell adhesion directed sorting out of low E-cadherin surface-derived cells from high E-cadherin interior cells (*21*). Low cell-cell adhesion strength between surface cells likely also contributed to their increased motility (*17*) and facilitated reinsertion of returning cells. Reinserted cells might be stabilized at the surface by strong cell-matrix adhesions to the basement membrane, as proposed in our model (**Fig. 2E**). In this testable model, provisional surface cells are first generated by proliferation of surface cells and temporarily stored in the interior domain. These cells are then returned to the surface layer by sorting based on differential cell-cell adhesion, reinsert between surface cells adhering weakly to each other and use strong cell-matrix adhesions to remain adherent to the basement membrane (**Fig. 2E**).

To test this model, we first derived numerical constraints for cell proliferation ratios (α) and geometric ratios (β) between interior and surface-layer domains of an inflating sphere (or oblate sphere) (**Fig. S4A-B**). An important assumption was compartmentalization between interior and

bioRxiv preprint doi: https://doi.org/10.1101/2020.06.24.165795; this version posted June 24, 2020. The copyright holder for this preprint (which was not certified by peer review) is the author/funder, who has granted bioRxiv a license to display the preprint in perpetuity. It is made available under aCC-BY-NC-ND 4.0 International license.

surface domains, based on the observed clear separation of peripheral vs. interior epithelial cells (**Movies 5-6**) with robust surface return of surface-derived proliferated interior cells (**Fig. 2B, Fig. S3C-D**). This model predicts that extra surface will fold to maintain tissue integrity when the surface expands faster than the interior (Scenario II; **Fig. S4C**), as observed during salivary gland branching. We then estimated actual proliferation ratios (α) and geometric ratios (β) by immunostaining cell proliferation and morphology markers in branching salivary glands (**Fig. S4D-E**). We found that all data mapped to the parameter space permissive for surface folding (Scenario II; **Fig. S4F**), supporting our proposed model.

Another prediction of our model is that if the number of stored interior proliferating cells could be increased, it might be possible to accumulate "branching potential" separate from actual branching (**Fig. 2E**). We tested this by treating salivary glands with collagenase to disrupt the major basement membrane component collagen IV. Collagenase treatment virtually ablated collagen IV and greatly reduced laminin in basement membranes (**Fig. S5A**). Existing epithelial buds fused together to revert branching (*22*) (**Fig. 2F-G, Fig. S5B**). Importantly, we discovered greatly accelerated catch-up branching after collagenase washout (**Fig. 2F-G, Fig. S5B-C**) likely resulting from attaching of accumulated post-proliferation cells to the restored basement membrane. We conclude that basement membrane disruption can uncouple the buildup of an interior pool of surface cell daughters from subsequent surface expansion. Basement membrane restoration enables rapid surface expansion and branching due to basement membrane anchorage and expansion of the surface epithelial sheet from this built-up interior pool of daughter cells.

Our model suggests that stratified epithelial branching is driven by a population of cells with weak cell-cell adhesions plus strong cell-matrix adhesions. Reducing expression of cell-cell adhesion molecules can positively regulate branching morphogenesis in both mammary gland and embryonic pancreas (*8*, *23*), but whether it is sufficient to cause branching remained unknown. To address this question, we attempted to reconstitute epithelial branching by engineering cell adhesion. We chose the human colorectal adenocarcinoma cell line DLD-1 as a starting point, because DLD-1 expresses abundant E-cadherin and forms near-spherical spheroids under low-attachment 3D culture conditions (*24*). For sophisticated modulation of different cell adhesion molecules, we established a clonal DLD-1 cell line after introducing transgenes to enable CRISPR/dCas9-based inducible transcriptional repression and activation (*25*) (**Fig. S6A-C**). To stably express sgRNAs and simultaneously monitor their expression, we constructed lentiviral vectors co-expressing sgRNAs with bright nuclear fluorescent reporters (**Fig. S6D**).

To reduce cell-cell adhesion strength, we identified two Cdh1 sgRNAs (*26*) that efficiently reduced E-cadherin expression levels after cells were treated with abscisic acid (ABA), a dimerizer used to recruit the KRAB transcriptional repression domain (**Fig. 3A, Fig. S6E-F, J**). Without ABA, sg1-Cdh1 had minimal effects, whereas sg2-Cdh1 reduced E-cadherin to 20% of control (**Fig. S6E-F, J**), likely due to direct transcriptional blockade. Inhibiting E-cadherin in DLD-1 caused only moderate reduction of β-catenin (**Fig. S6G**) and did not reduce cell proliferation or survival as reported for breast cancer cells (*27*). The level of E-cadherin reduction could be titrated by ABA concentrations, approaching maximum reduction at 3 days for sg1-Cdh1 and 2 days for sg2-Cdh1 (**Fig. S6H-I**). Importantly, we observed sorting out of low-E-cadherin cells in spheroid cultures of mixed sg-Control and sg-Cdh1 cells, suggesting E-cadherin reduction successfully lowered cell-cell adhesion strength (**Fig. S7A**).

DLD-1 spheroids failed to spontaneously form a basement membrane (data not shown), a structure critical for salivary gland branching (**Fig. S5**). To induce basement membrane formation, we supplemented culture media with a soluble suspension of the basement membrane extract Matrigel (*28*). Strikingly, this led to robust branching in spheroid cultures containing sg1-

bioRxiv preprint doi: https://doi.org/10.1101/2020.06.24.165795; this version posted June 24, 2020. The copyright holder for this preprint (which was not certified by peer review) is the author/funder, who has granted bioRxiv a license to display the preprint in perpetuity. It is made available under aCC-BY-NC-ND 4.0 International license.

Cdh1 or sg2-Cdh1 cells after ABA-induced E-cadherin reduction (**Fig. 3B-F, Fig. S7B-F; Movie S8**). Importantly, a condensed layer of basement membrane had formed around the spheroids with high levels of the basement membrane components laminin and collagen IV (**Fig. 3G-H**). In spheroids containing both sg-Cdh1 and sg-Control cells, cells contacting the basement membrane were primarily sg-Cdh1 cells lacking E-cadherin expression (**Fig. 3H, Fig. S8A**). Furthermore, live-spheroid imaging revealed a similar mode of cleft formation as in salivary glands (**Fig. 3I; Movie S9**). Bud formation could occur in spheroids containing only low-E-cadherin sg-Cdh1 cells, but it was more robust when mixed with high-E-cadherin sg-Control cells (**Fig. S7G-H**). Furthermore, the combinations of estimated proliferation and geometric ratios of interior to surface domains in reconstituted spheroids predicted the observed surface folding (**Fig. S8A-D**). Summarizing the process of reconstituted branching, cells with experimentally reduced E-cadherin expression sorted out to the surface by differential cell-cell adhesion and then interacted with the basement membrane to promote branching as strong cell-matrix adhesions displaced weak cell-cell adhesions (**Fig. S8E**).

Our model predicts that strong cell-matrix interactions are required for branching in reconstituted spheroids. We tested this by inhibiting cell-matrix interactions using a function-blocking β1-integrin antibody, which inhibited bud formation (**Fig. S9A**). We confirmed that β1-integrin-dependent cell-matrix interactions were specifically required in low-E-cadherin cells using an Itgb1 sgRNA that efficiently reduced β1-integrin expression after ABA-enhanced transcriptional repression (**Fig. S9B-D**). Bud formation was completely blocked when sg-Itgb1 was expressed in low-E-cadherin cells or in all cells, but not in only high-E-cadherin cells (**Fig. 4A-C; Fig. S9E**), demonstrating that β1-integrin-dependent cell-matrix interactions were specifically required in low-E-cadherin cells. Importantly, reducing E-cadherin or β1-integrin expression did not affect expression of each other, and they selectively inhibited cell attachment to E-cadherin extracellular domain or Matrigel-coated surfaces, respectively (**Fig. S10**).

We next tested whether enhancing cell-matrix adhesion strength could enhance branching. We capitalized on the low-level bud formation observed in mixed sg-Control/sg2-Cdh1 spheroid cultures without ABA, providing a sensitized assay (**Fig. S7C-F**). Using $MnCl_2$ to enhance integrin-mediated cell-matrix adhesion strength (*29*) produced a modest but definitive increase in bud formation (**Fig. 4D-E; Fig. S9F**). Thus, enhancing cell-matrix adhesion strength can enhance branching.

Discussion

Besides holding cells together to form multicellular tissues, cell-cell and cell-matrix adhesions play important additional roles in tissue morphogenesis. For example, differential cell-cell adhesion promotes cell sorting (*21*), whereas differing cell-matrix interactions between cell types can override the influence of cell-cell interactions to provide alternative self-organization strategies (*30*). In both scenarios, tissues are driven toward states that minimize the systemic interfacial energy by maximizing interfaces with stronger interactions. Following related biophysical principles, our work establishes that strong cell-matrix adhesions associated with weak cell-cell adhesions are sufficient to drive cleft and bud formation, the early steps of stratified epithelial branching morphogenesis. Our in vitro spheroid model provides an experimental platform to explore mechanisms of later steps, e.g., ductal differentiation.

Importantly, our view of clefting in stratified epithelia as folding of an expanding surface cell sheet reveals hidden similarities between the seemingly discrepant branching mechanisms used by single-layered and stratified epithelia. Both can now be viewed as buckling of an epithelial sheet, except that the surface cell sheet in a stratified epithelium is more cryptic, moves inward rather than outward, and is mainly constrained by the interior epithelium rather than the

bioRxiv preprint doi: https://doi.org/10.1101/2020.06.24.165795; this version posted June 24, 2020. The copyright holder for this preprint (which was not certified by peer review) is the author/funder, who has granted bioRxiv a license to display the preprint in perpetuity. It is made available under aCC-BY-NC-ND 4.0 International license.

surrounding mesenchyme. This should facilitate development of unifying physical models of epithelial branching morphogenesis.

References and Notes:

1. S. Wang, R. Sekiguchi, W. P. Daley, K. M. Yamada, Patterned cell and matrix dynamics in branching morphogenesis. *J. Cell Biol.* **216**, 559–70 (2017).
2. V. N. Patel, I. T. Rebustini, M. P. Hoffman, Salivary gland branching morphogenesis. *Differentiation*. **74**, 349–64 (2006).
3. M. Affolter, R. Zeller, E. Caussinus, Tissue remodelling through branching morphogenesis. *Nat. Rev. Mol. Cell Biol.* **10**, 831–42 (2009).
4. F. Costantini, R. Kopan, Patterning a complex organ: Branching morphogenesis and nephron segmentation in kidney development. *Dev. Cell*. **18** (2010), pp. 698–712.
5. H. P. Shih, A. Wang, M. Sander, Pancreas organogenesis: from lineage determination to morphogenesis. *Annu. Rev. Cell Dev. Biol.* **29**, 81–105 (2013).
6. M. Larsen, C. Wei, K. M. Yamada, Cell and fibronectin dynamics during branching morphogenesis. *J. Cell Sci.* **119**, 3376–84 (2006).
7. A. J. Ewald, A. Brenot, M. Duong, B. S. Chan, Z. Werb, Collective epithelial migration and cell rearrangements drive mammary branching morphogenesis. *Dev. Cell*. **14**, 570–81 (2008).
8. H. P. Shih, D. Panlasigui, V. Cirulli, M. Sander, ECM signaling regulates collective cellular dynamics to control pancreas branching morphogenesis. *Cell Rep.* **14**, 169–79 (2016).
9. H. Nogawa, Y. Takahashi, Substitution for mesenchyme by basement-membrane-like substratum and epidermal growth factor in inducing branching morphogenesis of mouse salivary epithelium. *Development*. **112**, 855–61 (1991).
10. H. Nogawa, T. Ito, Branching morphogenesis of embryonic mouse lung epithelium in mesenchyme-free culture. *Development*. **121**, 1015–22 (1995).
11. H. Y. Kim, M.-F. Pang, V. D. Varner, L. Kojima, E. Miller, D. C. Radisky, C. M. Nelson, Localized smooth muscle differentiation is essential for epithelial bifurcation during branching morphogenesis of the mammalian lung. *Dev. Cell*. **34**, 719–26 (2015).
12. C. M. Nelson, On buckling morphogenesis. *J. Biomech. Eng.* **138**, 1–6 (2016).
13. K. Goodwin, S. Mao, T. Guyomar, E. Miller, D. C. Radisky, A. Košmrlj, C. M. Nelson, Smooth muscle differentiation shapes domain branches during mouse lung development. *Development*. **146**, 1–13 (2019).
14. R. J. Metzger, O. D. Klein, G. R. Martin, M. A. Krasnow, The branching programme of mouse lung development. *Nature*. **453**, 745–50 (2008).
15. E. E. Morrisey, B. L. M. Hogan, Preparing for the first breath: Genetic and cellular mechanisms in lung development. *Dev. Cell*. **18**, 8–23 (2010).
16. R. J. Huebner, T. Lechler, A. J. Ewald, Developmental stratification of the mammary epithelium occurs through symmetry-breaking vertical divisions of apically positioned luminal cells. *Development*. **141**, 1085–94 (2014).
17. J. C. Hsu, H. Koo, J. S. Harunaga, K. Matsumoto, A. D. Doyle, K. M. Yamada, Region-specific epithelial cell dynamics during branching morphogenesis. *Dev. Dyn.* **242**, 1066–

bioRxiv preprint doi: https://doi.org/10.1101/2020.06.24.165795; this version posted June 24, 2020. The copyright holder for this preprint (which was not certified by peer review) is the author/funder, who has granted bioRxiv a license to display the preprint in perpetuity. It is made available under aCC-BY-NC-ND 4.0 International license.

77 (2013).

18. H. Tsutsui, S. Karasawa, H. Shimizu, N. Nukina, A. Miyawaki, Semi-rational engineering of a coral fluorescent protein into an efficient highlighter. *EMBO Rep.* **6**, 233–8 (2005).

19. L. Zhang, N. Stokes, L. Polak, E. Fuchs, Specific microRNAs are preferentially expressed by skin stem cells to balance self-renewal and early lineage commitment. *Cell Stem Cell*. **8**, 294–308 (2011).

20. J. L. Walker, A. S. Menko, S. Khalil, I. Rebustini, M. P. Hoffman, J. A. Kreidberg, M. A. Kukuruzinska, Diverse roles of E-cadherin in the morphogenesis of the submandibular gland: insights into the formation of acinar and ductal structures. *Dev. Dyn.* **237**, 3128–41 (2008).

21. M. S. Steinberg, Reconstruction of tissues by dissociated cells. *Science*. **141**, 401–8 (1963).

22. C. Grobstein, J. Cohen, Collagenase: effect on the morphogenesis of embryonic salivary epithelium in vitro. *Science*. **150**, 626–8 (1965).

23. K. V. Nguyen-Ngoc, K. J. Cheung, A. Brenot, E. R. Shamir, R. S. Gray, W. C. Hines, P. Yaswen, Z. Werb, A. J. Ewald, ECM microenvironment regulates collective migration and local dissemination in normal and malignant mammary epithelium. *Proc. Natl. Acad. Sci. U. S. A.* **109**, 19–24 (2012).

24. A. Riedl, M. Schlederer, K. Pudelko, M. Stadler, S. Walter, D. Unterleuthner, C. Unger, N. Kramer, M. Hengstschläger, L. Kenner, D. Pfeiffer, G. Krupitza, H. Dolznig, Comparison of cancer cells in 2D vs 3D culture reveals differences in AKT–mTOR–S6K signaling and drug responses. *J. Cell Sci.* **130**, 203–18 (2017).

25. Y. Gao, X. Xiong, S. Wong, E. J. Charles, W. A. Lim, L. S. Qi, Complex transcriptional modulation with orthogonal and inducible dCas9 regulators. *Nat. Methods*. **13**, 1043–9 (2016).

26. M. Haeussler, K. Schönig, H. Eckert, A. Eschstruth, J. Mianné, J.-B. Renaud, S. Schneider-Maunoury, A. Shkumatava, L. Teboul, J. Kent, J.-S. Joly, J.-P. Concordet, Evaluation of off-target and on-target scoring algorithms and integration into the guide RNA selection tool CRISPOR. *Genome Biol.* **17**, 148 (2016).

27. V. Padmanaban, I. Krol, Y. Suhail, B. M. Szczerba, N. Aceto, J. S. Bader, A. J. Ewald, E-cadherin is required for metastasis in multiple models of breast cancer. *Nature*. **573**, 439–44 (2019).

28. H. K. Kleinman, M. L. McGarvey, J. R. Hassell, V. L. Star, F. B. Cannon, G. W. Laurie, G. R. Martin, Basement membrane complexes with biological activity. *Biochemistry*. **25**, 312–8 (1986).

29. G. Bazzoni, D. T. Shih, C. A. Buck, M. E. Hemler, Monoclonal antibody 9EG7 defines a novel β1 integrin epitope induced by soluble ligand and manganese, but inhibited by calcium. *J. Biol. Chem.* **270**, 25570–7 (1995).

30. A. E. Cerchiari, J. C. Garbe, N. Y. Jee, M. E. Todhunter, K. E. Broaders, D. M. Peehl, T. A. Desai, M. A. LaBarge, M. Thomson, Z. J. Gartner, A strategy for tissue self-organization that is robust to cellular heterogeneity and plasticity. *Proc. Natl. Acad. Sci. U. S. A.* **112**, 2287–92 (2015).

31. A. K. Hadjantonakis, V. E. Papaioannou, Dynamic in vivo imaging and cell tracking using a histone fluorescent protein fusion in mice. *BMC Biotechnol.* **4**, 1–14 (2004).

bioRxiv preprint doi: https://doi.org/10.1101/2020.06.24.165795; this version posted June 24, 2020. The copyright holder for this preprint (which was not certified by peer review) is the author/funder, who has granted bioRxiv a license to display the preprint in perpetuity. It is made available under aCC-BY-NC-ND 4.0 International license.

32. M. D. Muzumdar, B. Tasic, K. Miyamichi, L. Li, L. Luo, A global double-fluorescent Cre reporter mouse. *Genesis*. **45**, 593–605 (2007).

33. S. J. Sequeira, E. M. Gervais, S. Ray, M. Larsen, Genetic modification and recombination of salivary gland organ cultures. *J. Vis. Exp.*, 1–7 (2013).

34. D. G. Gibson, L. Young, R.-Y. Chuang, J. C. Venter, C. A. Hutchison, H. O. Smith, Enzymatic assembly of DNA molecules up to several hundred kilobases. *Nat. Methods*. **6**, 343–5 (2009).

35. M. I. Pronobis, N. Deuitch, M. Peifer, The Miraprep: A protocol that uses a Miniprep kit and provides Maxiprep yields. *PLoS One*. **11**, 1–12 (2016).

36. S. K. Akiyama, Purification of fibronectin. *Curr. Protoc. Cell Biol.* **2**, 1–13 (1999).

37. J. Schindelin, I. Arganda-Carreras, E. Frise, V. Kaynig, M. Longair, T. Pietzsch, S. Preibisch, C. Rueden, S. Saalfeld, B. Schmid, J. Y. Tinevez, D. J. White, V. Hartenstein, K. Eliceiri, P. Tomancak, A. Cardona, Fiji: An open-source platform for biological-image analysis. *Nat. Methods*. **9**, 676–82 (2012).

38. J. Y. Tinevez, N. Perry, J. Schindelin, G. M. Hoopes, G. D. Reynolds, E. Laplantine, S. Y. Bednarek, S. L. Shorte, K. W. Eliceiri, TrackMate: An open and extensible platform for single-particle tracking. *Methods*. **115**, 80–90 (2017).

39. D. Legland, I. Arganda-Carreras, P. Andrey, MorphoLibJ: Integrated library and plugins for mathematical morphology with ImageJ. *Bioinformatics*. **32**, 3532–4 (2016).

Acknowledgments: We thank all members of the Yamada Laboratory for helpful discussions, J.W. Collins, D.A. Cruz Walma, A.D. Doyle, S.S. Nazari, D. Wu (NIDDK), J. Lu (Shandong University), A. Desai (UCSD), R.A. Green (UCSD), and K. Oegema (UCSD) for critical reading of the manuscript, A.D. Doyle from the NIDCR Imaging Core for assistance in microscopy, L. Zhang, G.T. McGrady and E. Stregevsky from the NIDCR Combined Technical Research Core for Sanger sequencing and cell sorting, the NIDCR Veterinary Resource Core for mouse care, S. Qi (Stanford University), F. Zhang (MIT), and D. Trono (EPFL) for plasmids, M.P. Hoffman (NIDCR), E. Fuchs (Rockefeller University) and A.J. Ewald (JHU) for mice. Image analysis was performed in part using the NIH High Performance Computing system. **Funding:** This work was supported by the NIH Intramural Research Program (NIDCR, ZIA DE000525). S.W. was supported in part by an NIDCR K99 Pathway to Independence Award (K99 DE27982). **Author contributions:** S.W. and K.M.Y. conceptualized the project. S.W. designed experiments with useful input from K.M. and K.M.Y.. S.W. and K.M. performed all experiments. S.W. performed data analysis with useful input from K.M. and K.M.Y.. All authors contributed to data interpretation. S.W. and K.M.Y. wrote the manuscript with useful input from K.M.. K.M.Y. acquired funding and supervised the project. **Competing interests:** Authors declare no competing interests. **Data and materials availability:** Data for reproducing all plots in this study are available in Figshare with the identifier [10.35092/yhjc.12145626 (reserved DOI); private link for peer review only: https://figshare.com/s/4d9ec0683d9f6d4ef951]. Raw data that support the findings of this study and biological materials such as plasmids, cell lines and mice are available from the corresponding author upon reasonable request. Customized scripts and usage instructions are available from Github: https://github.com/snownontrace/public-scripts-Wang2020-branching-morphogenesis .

bioRxiv preprint doi: https://doi.org/10.1101/2020.06.24.165795; this version posted June 24, 2020. The copyright holder for this preprint (which was not certified by peer review) is the author/funder, who has granted bioRxiv a license to display the preprint in perpetuity. It is made available under aCC-BY-NC-ND 4.0 International license.

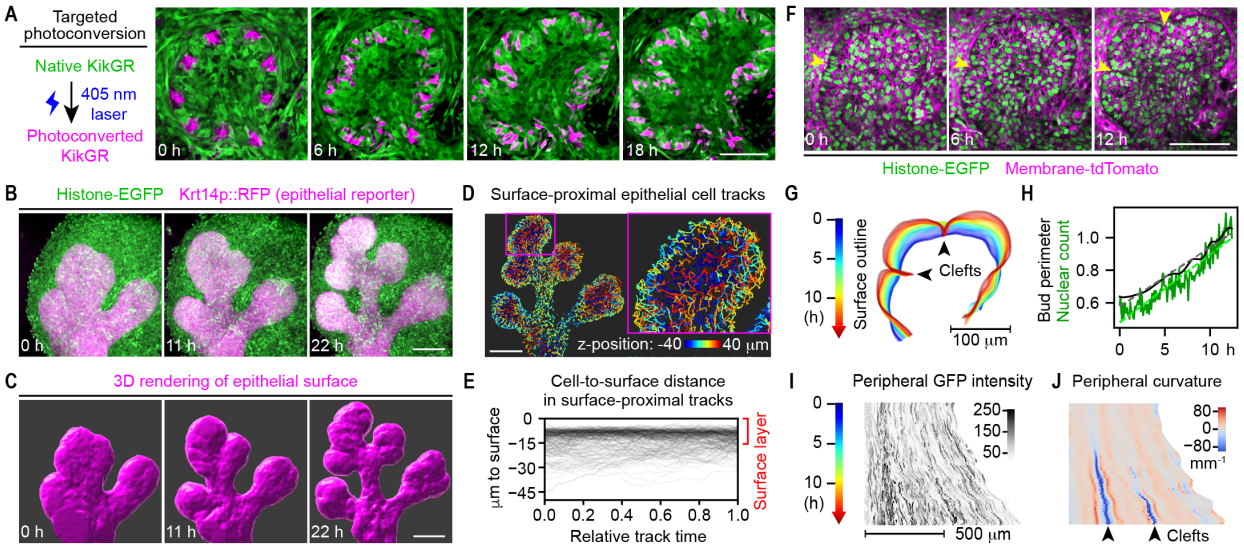

Fig. 1. Clefting in salivary glands is caused by uniform expansion and inward folding of the surface cell sheet. (**A**) Left: schematic of KikGR photoconversion; Right: snapshot confocal images showing the middle slice of a branching epithelial bud in an E13 mouse salivary gland expressing KikGR. (**B**) Time-lapse two-photon microscopy images showing the maximum intensity projection of an E12.5 transgenic mouse salivary gland. (**C**) 3D rendering of epithelial surface using Krt14p::RFP at time points matching the images in (B). (**D**) Surface-proximal epithelial cell tracks (tracking nuclear Histone-EGFP) color-coded by their z-position at 20-22 hours of the time-lapse sequence. Only epithelial cell tracks whose closest distance to the surface was ≤ 15 μm are shown. (**E**) Plot of the cell nucleus-to-surface distance versus time for 250 randomly selected 3-10 hour-long surface-proximal tracks. (**F**) Time-lapse two-photon microscopy images showing the middle slice of an E13 transgenic mouse salivary gland. (**G**) Outlines of the epithelial surface at the middle two-photon image slice over 12.5 hours at 5-min intervals. Blue to red, 0 to 12.5 hours. (**H**) Plot of the bud perimeter and nuclear count along the surface cell layer at the middle slice over time. Dashed lines indicate fitted linear models. (**I** and **J**) Heatmaps of GFP intensity (I) and the curvature (J) along the surface epithelial cell layer at the middle slice over time. Arrowheads in (F, G, J) indicate clefts. Scale bars, 100 μm.

bioRxiv preprint doi: https://doi.org/10.1101/2020.06.24.165795; this version posted June 24, 2020. The copyright holder for this preprint (which was not certified by peer review) is the author/funder, who has granted bioRxiv a license to display the preprint in perpetuity. It is made available under aCC-BY-NC-ND 4.0 International license.

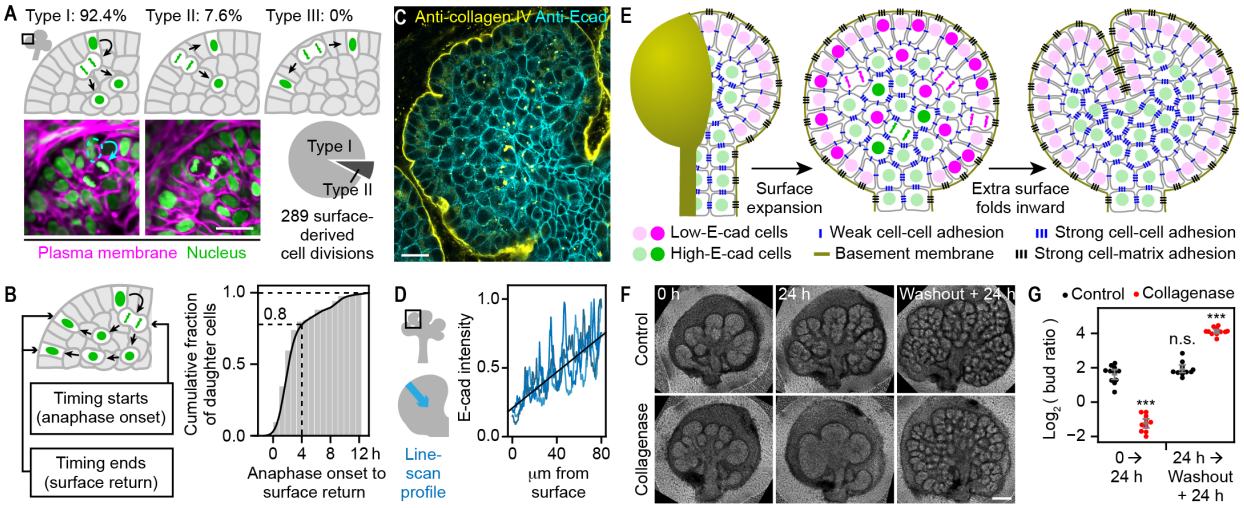

Fig. 2. Expansion of the surface cell sheet is driven primarily by subsurface cell division and reinsertion as new surface cells. (**A**) Top and bottom left: schematics and time-lapse two-photon microscopy images of 3 types of surface-derived cell division; Bottom right: pie chart showing proportions of the two observed types. (**B**) Schematic and cumulative distribution plot of time intervals from anaphase onset of mother cell division to returning of 84 daughter cells to the epithelial surface. (**C**) Confocal immunofluorescence image showing the middle slice of an epithelial bud from an E13.5 mouse salivary gland. (**D**) Schematic and plot of the surface-to-center line-scan profile of E-cadherin intensity. (**E**) Schematic model of clefting in a stratified epithelium. First, the surface layer expands by surface cell division and back-insertion. Second, the extra surface folds inward to produce clefting. Note that the two steps happen concurrently but are drawn separately for clarity. (**F**) Phase contrast images of E12 + 1.5-day cultured salivary glands (0 h) treated for 24 hours with solvent control or 20 µg/mL collagenase (24 h), followed by another 24 hours after washout (washout + 24 h). (**G**) Plot of log2 bud ratio over the indicated 24 h period. N=11 for each group. ***, Tukey test p<0.001. n.s., not significant. Scale bars, 20 µm in (A, C); 200 µm in (F).

bioRxiv preprint doi: https://doi.org/10.1101/2020.06.24.165795; this version posted June 24, 2020. The copyright holder for this preprint (which was not certified by peer review) is the author/funder, who has granted bioRxiv a license to display the preprint in perpetuity. It is made available under aCC-BY-NC-ND 4.0 International license.

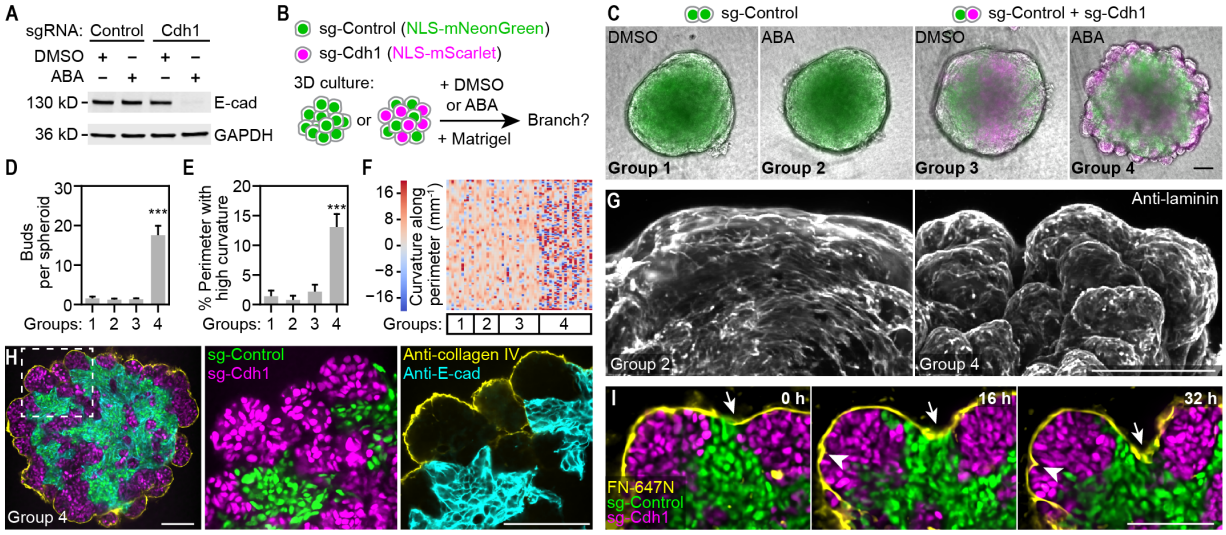

Fig. 3. Reconstitution of stratified epithelial branching. (**A**) Western blot of clonal Dia-C6 cells expressing Control (lacZ) or Cdh1 sgRNA treated with abscisic acid (ABA) or DMSO (vehicle). ABA is a dimerizer used to induce robust transcriptional repression in engineered cells. (**B**) Schematic of experimental design. (**C**) Merged phase contrast and epifluorescence images of spheroids from indicated experimental groups. (**D** and **E**) Bar plots of bud number or percentage of high-curvature perimeter length (|curvature|>20 mm^{-1}). Error bars, 95% confidence intervals. ***, Tukey test $p < 0.001$. (**F**) Heatmap showing color-coded curvature along spheroid perimeters. Each column is one spheroid. Sample numbers in (C to F): n=11, 10, 16, 43 for groups 1-4 combining 2 independent experiments with similar results; only 21 randomly selected Group 4 samples were plotted in (F) to save space. (**G**) Maximum intensity projection of two-photon microscopy images of spheroids immunostained with laminin, a basement membrane marker. (**H**) Confocal images of a spheroid at the central slice. (**I**) Time-lapse confocal images of a branching spheroid. Atto-647N-labeled fibronectin was used to mark the basement membrane (yellow); arrows and arrowheads indicate clefts. Scale bars, 100 μm.

bioRxiv preprint doi: https://doi.org/10.1101/2020.06.24.165795; this version posted June 24, 2020. The copyright holder for this preprint (which was not certified by peer review) is the author/funder, who has granted bioRxiv a license to display the preprint in perpetuity. It is made available under aCC-BY-NC-ND 4.0 International license.

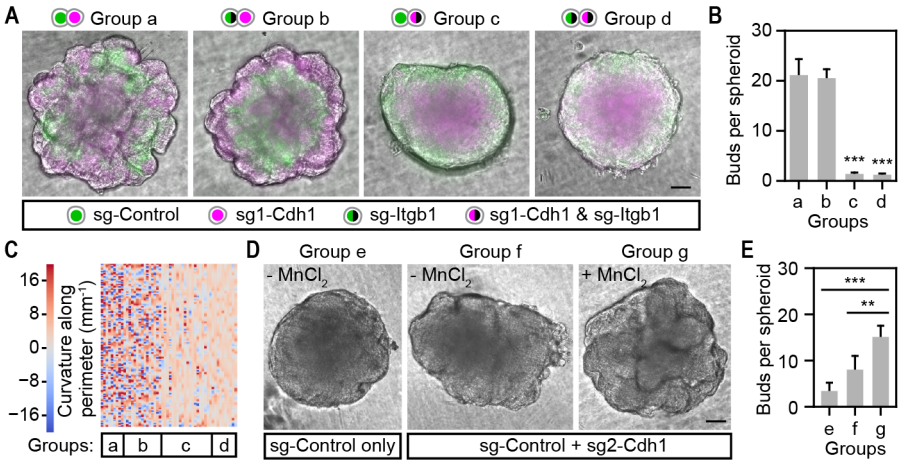

Fig. 4. Reconstituted epithelial branching depends on integrin-mediated cell-matrix adhesion. (**A**) Merged phase contrast and epifluorescence images of spheroids from indicated experimental groups. (**B**) Bar plot of bud number per spheroid. (**C**) Heatmap showing color-coded curvature along spheroid perimeters. Each column is one spheroid. (**D**) Phase contrast images of spheroids from indicated experimental groups. 50 μM $MnCl_2$ was used to enhance integrin-mediated cell-matrix adhesion. (**E**) Bar plot of bud number per spheroid. Sample numbers: n=9, 15, 20, 10, 10, 10, 20 for groups a-g from one of two independent experiments with similar results. Error bars in (B, C, F), 95% confidence intervals. **, ***, Tukey test $p < 0.01$ or $p < 0.001$. Scale bars, 100 μm.

bioRxiv preprint doi: https://doi.org/10.1101/2020.06.24.165795; this version posted June 24, 2020. The copyright holder for this preprint (which was not certified by peer review) is the author/funder, who has granted bioRxiv a license to display the preprint in perpetuity. It is made available under aCC-BY-NC-ND 4.0 International license.

Materials and Methods

Mice

All mouse experiments were performed under animal study protocols 14-745 and 17-845 approved by the NIDCR Animal Care and Use Committee (ACUC). All mouse embryos were used without sex identification (mixed sexes). All transgenic mice were in FVB/N background. The mT/mG;Histone-EGFP (*16*, *31*, *32*) mouse was a gift from A.J. Ewald (Johns Hopkins University). The Krt-14p::RFP (*19*) mouse was a gift from M.P. Hoffman (NIDCR, NIH) and was originally from E. Fuchs (Rockefeller University). Krt-14p::RFP mice were crossed with mT/mG;Histone-EGFP mice to generate Krt-14p::RFP;Histone-EGFP mice. Our KikGR mouse was generated as described (*17*). Transgenic mice 8-16 weeks old were bred to obtain 12- or 13-day old embryos. For timing of embryonic stage, the day after a vaginal plug was found was considered to be embryonic day 1. For experiments using wildtype embryos, timed pregnant ICR (CD1) outbred mice were obtained from Envigo.

Cell lines

The HEK293T cell line used for lentivirus packaging was obtained from Takara (632273). The DLD-1 cell line was obtained from ATCC (CCL-221). DLD-1 cells were co-transfected with a PiggyBac transposase vector (System Biosciences, PB210PA-1) and a PiggyBac-ABA-CRISPRi vector (*25*) (pSLQ2818; Addgene, 84241) using Lipofectamine 3000 (Thermo Fisher Scientific, L3000015), selected by 5 µg/mL puromycin (MilliporeSigma, P8833) and sorted for the presence of tagBFP to generate “Di” cells. Di cells were co-transfected with the above transposase vector, PiggyBac-ABA-CRISPRi vector and a modified PiggyBac-GA-CRISPRa vector (pW210, see Plasmids) using Lipofectamine 3000, selected by 5 µg/mL puromycin and 250 µg/mL hygromycin (MilliporeSigma, H3274) and sorted for brighter tagBFP than Di cells to generate “Dia” cells. Single cell clones of Dia cells were isolated by limiting dilution and selected clones were functionally validated. The clonal Dia-C6 cells were used for lenti-sgRNA transduction followed by 20 µg/mL blasticidin (InvivoGen, ant-bl-1) selection and fluorescence cell sorting for mNeonGreen or mScarlet (see Plasmids) to obtain final DLD-1 derived cell lines used for spheroid culture experiments.

Antibodies

Rabbit monoclonal E-cadherin antibody (Cell Signaling, 3195S) was used at 1:200 for immunostaining shown in **Fig. S10C**. Rat monoclonal E-cadherin antibody (Thermo Fisher, 13-1900) was used at 1 µg/mL for all other E-cadherin immunostaining and at 0.5 µg/mL for Western blotting. Anti-β1-integrin (in-house clone mAb13; available from MilliporeSigma, MABT821) was used at 100 µg/mL for function blocking and 1 µg/mL for immunostaining and Western blotting. Anti-α5-integrin (in-house clone mAb16; available from MilliporeSigma, MABT820) was used at 100 µg/mL as a control in the β1-integrin function blocking experiment. Other primary antibodies used for immunostaining: anti-collagen type IV (MilliporeSigma, AB769), 2 µg/mL; anti-laminin (MilliporeSigma, L9393), 2.5 µg/mL; anti-histone H3 (phospho S10) (Abcam, ab47297), 1 µg/mL; anti-Ki67 (MilliporeSigma, MAB4190), 2 µg/mL. Other primary antibodies used for Western blotting: anti-β-catenin (Abcam, ab32572), 1:5,000 (0.0126 µg/mL); anti-GAPDH (Cell Signaling, 2118L), 1:2,000; anti-α-tubulin (MilliporeSigma, T6199), 0.5 µg/mL. All immunostaining secondary antibodies were from Jackson ImmunoResearch (an equal volume of glycerol was added for storage at -20°C after reconstitution as instructed) and used at 1:200 (1.5-3 µg/mL): DyLight 405 donkey anti-rabbit (711-476-152), Cy2 donkey anti-goat (705-225-147), Alexa Fluor 488 donkey

bioRxiv preprint doi: https://doi.org/10.1101/2020.06.24.165795; this version posted June 24, 2020. The copyright holder for this preprint (which was not certified by peer review) is the author/funder, who has granted bioRxiv a license to display the preprint in perpetuity. It is made available under aCC-BY-NC-ND 4.0 International license.

anti-rat (712-546-153), Rhodamine Red-X donkey anti-rat (712-296-153), Rhodamine Red-X donkey anti-rabbit (711-296-152), Alexa Fluor 647 donkey anti-rat (712-606-153), Alexa Fluor 647 donkey anti-rabbit (711-606-152). All Western blotting secondary antibodies were from LI-COR and used at 1:5,000 for 800CW conjugates and 1:10,000 for 680RD conjugates: 680RD goat anti-rabbit (926-68071), 800CW goat anti-rat (926-32219), 680RD goat anti-mouse (926-68070), 800CW goat anti-rabbit (926-32211).

Salivary gland isolation and culture

Mouse submandibular salivary glands were isolated at embryonic day 12 or 13 (E12 or E13) as previously described (*33*), and cultured on 13 mm diameter polycarbonate filters (MilliporeSigma, WHA110405) floating on 200 µL Organ Culture Medium in the glass bottom area of a 50 mm MatTek dish (MatTek, P50G-1.5-14-F) at 37°C with 5% CO_2. Organ Culture Medium was DMEM/F-12 (Thermo Fisher, 11039047) supplemented with 150 µg/mL vitamin C (MilliporeSigma, A7506), 50 µg/mL transferrin (MilliporeSigma, T8158) and 1× PenStrep (100 units/mL penicillin, 100 µg/mL streptomycin; Thermo Fisher, 15140163).

Salivary gland collagenase treatment and washout

The left and right salivary glands from the same embryo were separated into control and collagenase treatment groups. Purified collagenase (Elastin Products Company, CL103) was resuspended in water (Quality Biological, 351-029-131) for a 2 mg/mL stock (stored at -20°C). 20 µg/mL collagenase (water as control) was used for salivary gland treatment. For collagenase washout, the polycarbonate filter with attached glands was transferred onto 2 mL fresh DMEM/F-12 in a 35 mm dish (Corning, 430165) and incubated for 15 min at 37°C for one wash. After 3× 15-min washes, the filter with glands was transferred onto 200 µL fresh Organ Culture Medium in a new 50 mm MatTek dish (see Salivary gland isolation and culture).

Cell culture

DMEM (Thermo Fisher, 11965118) and RPMI-1640 (ATCC, 30-2001) media were supplemented with 10% fetal bovine serum (FBS; GE Healthcare/Cytiva, SH30070.03), 2 mM L-glutamine (Thermo Fisher, 25030081) and 1× PenStrep to make DMEM Complete and RPMI-1640 Complete media. Phenol red free DMEM (GE Healthcare/Cytiva, SH30284.01) or RPMI-1640 (Thermo Fisher, 11835030) were used when cells were used for imaging or cell sorting. HEK293T cells were cultured in DMEM Complete medium in 37°C incubators with 10% CO_2. DLD-1 and DLD-1 derived cells were cultured in RPMI-1640 Complete medium in 37°C incubators with 5% CO_2. For passage, cells were detached using trypsin-EDTA (Thermo Fisher, 25300120) after rinsing with HBSS (Thermo Fisher, 14170161). Cell density was determined using an automated cell counter (Nexcelom Cellometer Auto 2000).

3D spheroid culture

Ultra-low attachment 96-well U-bottom (Corning, 7007) or V-bottom (S-bio, MS-9096VZ) plates were used for 3D spheroid culture. DLD-1 cells expressing different sgRNAs were detached, pelleted by centrifugation at 1,000×g for 3 min, resuspended in RPMI-1640 Complete medium, counted and diluted to 6×10^4 cells/mL. For co-cultures of two cell types (e.g., sg-Control and sg-Cdh1 cells), appropriate volumes of the two cells were mixed in a separate tube to achieve desired mixing ratios. A multichannel pipette (Rainin, 17013810) was used to seed 50 µL cell suspensions in each well for 3,000 cells per spheroid. The 36 outer edge wells were filled with 100 µL HBSS to reduce medium evaporation over long culture periods (≥ 7 days). Immediately after seeding,

bioRxiv preprint doi: https://doi.org/10.1101/2020.06.24.165795; this version posted June 24, 2020. The copyright holder for this preprint (which was not certified by peer review) is the author/funder, who has granted bioRxiv a license to display the preprint in perpetuity. It is made available under aCC-BY-NC-ND 4.0 International license.

the plate was centrifuged at 100×g for 3 min to sediment the cells. Next day, a 2× treatment mix of 44.8 μL RPMI-1640 Complete medium, 5 μL growth factor-reduced Matrigel (Corning, 356231; 9-10 mg/mL) and 0.2 μL DMSO (MilliporeSigma, D2650) or 50 mM abscisic acid (ABA; MilliporeSigma, A1049) was prepared for each well. A multichannel pipette was used to add 50 μL 2× treatment mix in each well for a final concentration of 5% Matrigel (450-500 μg/mL) and 100 μM ABA. Care was taken to minimize bubbles during pipetting. For integrin stimulation by $MnCl_2$, 0.1 μL 50 mM $MnCl_2$ was supplemented to every 50 μL 2× treatment mix. For integrin antibody blocking, two rat monoclonal antibodies (mAb13: anti-β1-integrin; mAb16: anti-α5-integrin) were diluted to 0.5 mg/mL in RPMI-1640 and passed through a desalting spin column (Thermo Fisher, 89883) pre-equilibrated for 4 times with RPMI-1640. Antibody concentrations were re-measured by absorbance at 280 nm on a nanodrop spectrophotometer (Denovix, DS-11). The per-well 2× treatment mix was adjusted to include 20 μL 0.5 mg/mL antibody solution, 19.4 μL RPMI-1640, 4.5 μL FBS, 0.45 μL 200 mM L-glutamine, 0.45 μL 100× PenStrep, 5 μL Matrigel and 0.2 μL 50 mM ABA.

Plasmids

The modified PiggyBac-GA-CRISPRa vector (pW210) was generated by replacing the Zeocin resistance cassette of pSLQ2842 (Addgene, 84244) with a synthesized Hygromycin resistance cassette (IDT) by Gibson Assembly (*34*). Lentiviral vectors for co-expressing sgRNAs and fluorescent nuclear reporters (pLenti-spsg-mNG/pW211, pLenti-spsg-mSL/pW212) were made by replacing the Cas9 expression cassette of lentiCRISPR v2 (Addgene, 52961) with an NLS-mNeonGreen-P2A-BlastR or NLS-mScarlet-I-BlastR cassette using Gibson Assembly. For lenti-sgRNA cloning, a pair of complementary oligos containing the desired sgRNA sequence (see sgRNA design) plus a 4-bp 5'-extension ("cacc" for the forward oligo and "aaac" for the reverse complementary oligo) was annealed to form an oligo duplex, which was ligated into Esp3I (NEB, R0734S) digested vectors by a 1:2 mixture of T4 ligase (NEB, M0202L) and T4 polynucleotide kinase (NEB, M0236L) in T4 ligase buffer. The ligation mix was transformed using NEB stable competent cells (NEB, C3040) for single colony isolation. The Miraprep (*35*) protocol was used to increase the yield of miniprep DNA, which was directly used for lentivirus packaging. Correct insertion of sgRNA sequence was confirmed by Sanger sequencing using primer 5'-gagggcctatttcccatgat-3'.

sgRNA design

sgRNAs for target genes (Cdh1 or Itgb1) were designed on the CRISPOR (*26*) website using 500 bp sequences centered around the transcription start site (TSS ± 250 bp). sg1-Cdh1: 5'-gCCGAGAGGCTGCGGCTCCAA-3'. sg2-Cdh1: 5'-gTGGCCGGGGACGCCGAGCGA-3'. sg-Itgb1: 5'-GGACGCCGCGCGGAAAAGGT-3'. Control guide RNAs for both the S. pyogenes Cas9 (5'-gTGCGAATACGCCCACGCGAT-3') and the S. aureus Cas9 (5'-gCCTTCCCAACAGTTGCGCAGC-3') were designed from the bacterial lacZ gene against the human genome. An extra "g" was added to the 5'-end if the guide sequence does not begin with "g" to facilitate transcription by the U6 promoter.

Lentivirus packaging

All lentivirus work was performed using BSL3 practices in a BSL2/3 room with a dedicated incubator. Lenti-sgRNA vectors (see Plasmids) were co-transfected with psPAX2 (Addgene, 12260) and pMD2.G (Addgene, 12259) into HEK293T cells by calcium co-precipitation to produce infectious lentiviral particles. Briefly, 4×10^6 HEK293T cells were seeded in a 10 cm dish one day before packaging. Next morning, culture media were changed and supplemented with 25 μM

bioRxiv preprint doi: https://doi.org/10.1101/2020.06.24.165795; this version posted June 24, 2020. The copyright holder for this preprint (which was not certified by peer review) is the author/funder, who has granted bioRxiv a license to display the preprint in perpetuity. It is made available under aCC-BY-NC-ND 4.0 International license.

chloroquine (MilliporeSigma, C6628). Two 15 mL tubes (A and B) were used to prepare the transfection mix. 1 mL 2× HBS (50 mM HEPES, 280 mM NaCl, 1.5 mM Na_2HPO_4, pH 7.10) was added to tube A. 10 µg of each plasmid (the lenti-sgRNA vector, psPAX2 and pMD2.G) and 1 mL 0.3 M $CaCl_2$ were sequentially added to tube B and mixed by pipetting. The DNA-$CaCl_2$ mixture in tube B was then added dropwise into the 2× HBS in tube A and mixed by pipetting. The transfection mix was then added dropwise to the 10 cm dish. Culture media were changed twice at about 12 and 36 hours post transfection, and lentivirus-containing media were collected twice at about 36 and 60 hours post transfection into a 50 mL tube (stored at 4°C). Pooled lentivirus-containing media were passed through a 0.45 µm filter (MilliporeSigma, SE1M003M00) to remove cell debris. To concentrate the lentivirus, 4 mL 5× PEG reagent (System Biosciences, LV825A-1) was added and mixed by pipetting. After ≥ 12 hours incubation at 4°C (up to 4 days), lentivirus was pelleted by centrifugation at 1,500× g for 30 min at 4°C, and the pellet was resuspended in 400 µL DMEM/F-12 with 1× PenStrep and stored at -80°C.

Lentivirus titration

The titer of concentrated lentivirus was estimated using Lenti-X GoStix Plus (Takara, 631281) after 100× dilution. A GoStix Value (GV) of 50 was empirically considered to be equivalent to a lentivirus titer of 5×10^5 IFU/mL. The typical titer of concentrated sgRNA lentivirus was 1.5×10^8 IFU/mL.

Lentivirus transduction

One day before transduction, 1×10^5 cells were seeded in a well of a 12-well plate. Next day, 2 µL 4 mg/mL polybrene (MilliporeSigma, H9268) was added to 1 mL medium (final 8 µg/mL). An appropriate amount of lentivirus for an MOI (multiplicity of infection; ratio of infectious viral particles to cells) of 10-15 (typically 20 µL for concentrated sgRNA lentivirus) was then added. One day later, the virus-containing medium was replaced with regular medium after 4× HBSS washes, and cells were re-plated to a 75 cm^2 flask in culture medium supplemented with 20 µg/mL blasticidin (InvivoGen, ant-bl-1) to begin the antibiotic selection.

Fluorescence activated cell sorting

For cell sorting, DLD-1 derived cells were trypsinized for 5 min longer than for passage (~15 min total) to increase the ratio of single cells, pelleted at 1,000× g for 3 min, and resuspended in phenol-red free, serum-free RPMI-1640 medium (Thermo Fisher, 11835030) for a cell density of 5-10 million/mL. The cell suspension was passed through a 40 µm Flowmi cell strainer (VWR, H13680-0040) and sorted on a BD FACSAria III or SONY SH800 cell sorter operated by the NIDCR Combined Technical Research Core.

Western blotting

DLD-1 derived cells were seeded in 12-well plates (Corning, 3512) at 2×10^4 cells/well on day 0, treated with DMSO vehicle or desired concentrations of ABA on day 1 (or each day of days 1-5 per well for an ABA time course), and harvested on day 6. Culture media were changed once on day 4 or 5. For harvesting, 100 µL RIPA buffer (25 mM Tris, pH 7.4, 150 mM NaCl, 1% NP-40, 0.5% sodium deoxycholate, 0.1% SDS) supplemented with protease inhibitors (MilliporeSigma, 11836170001) was added to each well after rinsing with PBS (Phosphate Buffered Saline; Lonza, 17-517Q). Cells were scraped into RIPA buffer on ice using 1 mL pipette tips. Cell suspensions were transferred to pre-cooled 1.5 mL tubes (Eppendorf, 022363212), incubated for 30 min on ice, and centrifuged at 13,000× rpm for 10 min at 4°C. Cleared cell lysates were transferred to a

bioRxiv preprint doi: https://doi.org/10.1101/2020.06.24.165795; this version posted June 24, 2020. The copyright holder for this preprint (which was not certified by peer review) is the author/funder, who has granted bioRxiv a license to display the preprint in perpetuity. It is made available under aCC-BY-NC-ND 4.0 International license.

new set of pre-cooled 1.5 mL tubes and stored at -20°C. Protein concentrations of cell lysates were determined by Bradford assays (Bio-Rad, 5000201). Lysate aliquots with 16 µg protein were denatured in 1× Laemmli sample buffer (Bio-Rad, 1610747) for 5 min at 95°C. Samples of 8 µg protein or 10 µL protein ladder (Thermo Fisher, 26623) were loaded per lane onto a precast gel (Bio-Rad, 4561096) for electrophoresis. Proteins were transferred onto a nitrocellulose membrane (Bio-Rad, 1704159) using the Turbo Transfer system (Bio-Rad, 1704150). The membrane was stained with Ponceau S (MilliporeSigma, P7170) to assess transfer quality, washed for 5 min in TBST (Tris Buffered Saline with 0.1% Tween-20; Quality Biological, 351-086-101; MilliporeSigma, P2287) to remove Ponceau staining, blocked in Blocking Solution (5% nonfat dry milk in TBST) for 30 min at room temperature (RT), incubated in primary antibodies (see Antibodies) diluted in Blocking Solution for overnight at 4°C, washed 4× 5 min with TBST at RT, incubated in LI-COR secondary antibodies (see Antibodies) diluted in Blocking Solution for 1-2 hours at RT, washed 4× 5 min in TBST at RT, and imaged on a LI-COR Odyssey CLx imaging system controlled by the LI-COR Image Studio software. Western blotting band intensities were quantified using LI-COR Image Studio Lite software.

Immunostaining of spheroids and salivary glands

Spheroids were rinsed in 2 mL PBS in a 35 mm dish and transferred into sample baskets (one basket per staining group; Intavis, 12.440) using low-retention pipette tips (cut for larger opening; Rainin, 30389187 or 30389190) under a dissecting microscope. For fixation, each basket was soaked in 1 mL fixative (4% PFA in PBS; Electron Microscopy Sciences, 15710) in a well of a 24-well plate (Corning, 3524) overnight at 4°C. Cultured salivary glands were fixed on the filter by replacing Organ Culture Medium under the filter with 200 µL fixative for 1 hour at room temperature (RT) or overnight at 4°C. Fixed glands were detached from the filter and transferred into sample baskets in PBS in a 35 mm dish using a pair of forceps (Fine Science Tools, 11252-23) under a dissecting microscope. Fixed samples in baskets were permeabilized in PBSTx (PBS with 0.2% Triton-X-100; Thermo Fisher, 28314) for 30 min at RT, blocked in 5% donkey serum (Jackson ImmunoResearch, 017-000-121) in PBSTx for 2 hours at RT, incubated in primary antibodies (see Antibodies) diluted in either PBSTx or 5% donkey serum for 2 days at 4°C, washed 4× 15 min in PBSTx at RT, incubated in secondary antibodies (see Antibodies) diluted in either PBSTx or 5% donkey serum for 2 days at 4°C, washed 4× 15 min in PBSTx at RT, rinsed in PBS and mounted under a dissecting microscope. To preserve fluorescence and to minimize compression, samples were mounted in 20 or 40 µL antifade mountant (Thermo Fisher, P36930) supported by one layer (for salivary glands) or two layers (for spheroids) of imaging spacers (Grace Bio-labs, 654004) attached to a glass slide (Thermo Fisher, 3011-002).

Tissue clearing of spheroids

Tissue clearing was performed for images shown in **Fig. 3G** to enable imaging over 200 µm thickness. For tissue clearing, regular immunostaining steps were carried out except for mounting. Spheroids were instead sequentially transferred to each well of a 3-well silicone chamber slide (ibidi, 80381), each containing 500 µL CytoVista clearing reagent (Thermo Fisher, V11315). After 5 min incubation in the last well, spheroids were transferred to 200 µL CytoVista clearing reagent per well of an 8-well glass-bottom ibidi chamber (ibidi, 80827) for imaging with two-photon microscopy (see Immunostaining light microscopy). Note that this clearing reagent preserved mScarlet but not mNeonGreen fluorescence.

Immunostaining of cells

bioRxiv preprint doi: https://doi.org/10.1101/2020.06.24.165795; this version posted June 24, 2020. The copyright holder for this preprint (which was not certified by peer review) is the author/funder, who has granted bioRxiv a license to display the preprint in perpetuity. It is made available under aCC-BY-NC-ND 4.0 International license.

Cells were seeded, immunostained and imaged in 8-well ibidi chambers (ibidi, 80826). All procedures were performed at room temperature with gentle rocking. Cells were fixed with 4% PFA in PBS for 15 min, permeabilized with PBSTx for 15 min, blocked in 5% donkey serum in PBS for 30 min, incubated in primary antibodies (see Antibodies) diluted in PBS for 1 hour, washed 4× 5 min with PBS, incubated in 0.5 µg/mL DAPI (Thermo Fisher, D1306) and secondary antibodies (see Antibodies) diluted in PBS for 1 hour, washed 4× 5 min with PBS, stored at 4°C and imaged within 3 days.

Cell attachment assay

DLD-1 derived cells (sg-Control, sg1-Cdh1, sg2-Cdh1 and sg-Itgb1) were pre-treated with 100 µM ABA for 5-10 days before being used. The glass surface of MatTek 6-well plates (MatTek, P06G-0-14-F) was coated with 200 µL 91 µg/mL Matrigel in PBS or 8 µg/mL E-cadherin extracellular domain (E-cad-ECD; R&D Systems, 8505-EC-050) in PBS for 1-3 hours at 37ºC. Coated wells were rinsed once with 3 mL PBS, blocked with 2 mL 5% bovine serum albumin (BSA; MilliporeSigma, 10735108001) in PBS for 30 min at 37ºC, and washed twice with 3 mL PBS. During the blocking step, cells were detached, pelleted, resuspended, counted and diluted to 5×10^4 cells/mL. 2 mL cell suspension was seeded in each well. 3 or 4 wells were used per experimental group. After 15 min (for Matrigel coating) or 2 hours (for E-cad-ECD coating) incubation at 37ºC with 5% CO_2, unattached cells were removed from each well, which was then gently washed 3× with 3 mL PBS, fixed with 2 mL 4% PFA in PBS for 15 min at 37ºC, washed 2× with 3 mL PBS, and imaged under a microscope (see Live-spheroid imaging and cell-attachment assay imaging) to quantify attached cell densities (see Image processing and analysis). For assay consistency, a 2 mL aspirating pipette was capped with a 200 µL pipette tip to attenuate vacuum strength, and the house vacuum valve was pre-adjusted using PBS to reach a liquid removal rate of ~1 mL/second. During liquid removal and addition, tips of aspirating or transferring pipettes were always placed to the side of the bottom of the MatTek well away from the coated glass surface, resulting in ~200 µL leftover liquid between washes. Care was taken throughout the assay to avoid agitating the plates. The incubation time for each coating was determined to be the time at which ~50% of control cells were attached in pilot assays.

Live-organ imaging by two-photon microscopy

All microscopy systems for live imaging were equipped with an environmental chamber to maintain samples at 37°C with 50% humidity and 5% CO_2. Transgenic salivary glands expressing fluorescent markers were isolated and cultured on a floating 13 mm filter at 37°C with 5% CO_2 (see Salivary gland isolation and culture) for at least 1 hour before being mounted for live imaging. Double-adhesive imaging spacers (Grace Bio-labs, 654008; cut into 8 separated wells, each 120 µm thick with 9 mm diameter opening) were sterilized by soaking in 70% ethanol for 3 min and attached to the glass bottoms of 50 mm MatTek dishes (MatTek, P50G-1.5-30-F). Under a dissecting microscope, 5 µL Organ Culture Medium was transferred to the center of the imaging spacer, and the filter with glands was flipped onto the imaging spacer so that glands were sandwiched between the filter and the glass bottom. Care was taken to ensure the filter was flat and center-aligned with the imaging spacer. The edge of the filter was pressed to ensure tight adherence to the imaging spacer. 2 mL Organ Culture Medium was then added to the MatTek dish, which was incubated at 37°C with 5% CO_2 for at least 2 hours before imaging. A Nikon 40×, 1.15 NA, Apo LWD, water-immersion objective or a Nikon 25×, 1.05 NA, Plan Apo, silicone-immersion objective was used for live-organ imaging using two-photon microscopy on a Nikon A1R Confocal Microscope System equipped with a Ti:sapphire laser (Coherent, Chameleon Vision II). Image acquisition was controlled by Nikon NIS-Elements software. Images were acquired at 2 µm z intervals over 100 µm thickness and 5 min intervals for 20-36 hours. The

bioRxiv preprint doi: https://doi.org/10.1101/2020.06.24.165795; this version posted June 24, 2020. The copyright holder for this preprint (which was not certified by peer review) is the author/funder, who has granted bioRxiv a license to display the preprint in perpetuity. It is made available under aCC-BY-NC-ND 4.0 International license.

tunable laser was used at 950 nm for simultaneous two-photon excitation of histone-EGFP and membrane-tdTomato (or heterozygous Krt14p::RFP), and 920 nm for histone-EGFP and homozygous Krt14p::RFP. The laser power was adjusted to compensate for z-depth changes using the "Z Intensity Correction" option with criteria that the bulk histograms of both channels spanned 500-1500 gray values (at typically 1-8% or 12-100 mW power).

KikGR photoconversion and live imaging by confocal microscopy

E13 KikGR transgenic glands were cultured on the filter with Organ Culture Medium supplemented with 5 µg/mL AF680-anti-collagen IV (see Protein labeling) for ~10 hours. Under a dissecting microscope, a 10 µL pipette tip was used to spot vacuum grease (MilliporeSigma, 18405) around glands on the filter, which was then flipped onto the glass area of a 35 mm dish (MatTek, P35G-1.5-20-C). The vacuum grease limited gland compression and also served as a bio-inert glue to adhere the filter to the glass. 2 mL Organ Culture Medium supplemented with 1 µg/mL AF680-anti-collagen IV (see Protein labeling) were added to the dish for imaging after 2 hours incubation at 37°C with 5% CO_2. A Nikon 40×, 1.15 NA, Apo LWD, water-immersion objective was used for photoconversion and imaging on a Nikon A1R Confocal Microscope System equipped with 4 laser lines (405 nm, 488 nm, 561 nm, 640 nm; Nikon LU-N4). Photoconversion and image acquisition were controlled by Nikon NIS-Elements software. For photoconversion, a 405 nm laser was used at 1-5% power (0.15-0.75 mW) with the pinhole set at 1 AU (Airy Unit; 30.7 µm) to stimulate user-specified polygonal ROIs (Regions of Interest) in the "ND Stimulation" module of the software. Short 1-5 second pulses (depending on ROI sizes) were repeated until all green fluorescence inside ROIs was converted to red fluorescence. For image acquisition, 488 nm and 561 nm lasers were used at 2% power (0.3 mW), whereas the 640 nm laser was used at 5% (0.75 mW) with the pinhole set at 1.2 AU (58.7 µm). Images were acquired at 10 min time intervals and 2 µm z intervals.

Live-spheroid imaging and cell-attachment assay imaging

Live-spheroid imaging (time-lapse or single-time-point) and cell-attachment assay imaging were performed by phase contrast and epifluorescence microscopy using a Nikon 10×, 0.3 NA, Plan Fluor objective on a Nikon Ti-E brightfield microscope system with a Hamamatsu Orca Flash 4.0 V3 sCMOS camera. Spheroids were imaged in the same 96-well U-bottom or V-bottom plates for culture. Image acquisition was controlled by Nikon NIS-Elements software. The JOBS module of the software was used to automatically set up multiple positions in a 96-well plate (spheroids) or a 6-well plate (cell attachment assay). For time-lapse live-spheroid imaging by confocal microscopy, spheroids were incubated in 40 µg/mL Atto647N-fibronectin (see Protein labeling) overnight at 37°C with 5% CO_2 and transferred into a 4-well 35 mm dish (ibidi, 80466), each well of which contained 2 or 3 spheroids in 100 µL spheroid culture medium with 10 µg/mL Atto647N-fibronectin. A Nikon 20×, 0.75 NA, Plan Apo objective was used on a Nikon A1R Confocal Microscope System equipped with 4 laser lines. A resonant scanner was used for high-speed laser scanning. Image acquisition was controlled by Nikon NIS-Elements software at 10 min time intervals and 2 µm z intervals.

Immunostaining light microscopy

Immunostained spheroids in **Fig. 3G** were imaged by two-photon microscopy using a Nikon 20×, 0.75 NA objective on a Nikon A1R Confocal Microscope System equipped with a Ti:sapphire laser (used at 760 nm, 3% or 90 mW) controlled by Nikon NIS-Elements software. All other immunostained spheroids and salivary glands were imaged by laser scanning confocal microscopy using Nikon 20×, 0.75 NA or 60×, 1.4 NA Plan Apo objectives on a Nikon A1R

bioRxiv preprint doi: https://doi.org/10.1101/2020.06.24.165795; this version posted June 24, 2020. The copyright holder for this preprint (which was not certified by peer review) is the author/funder, who has granted bioRxiv a license to display the preprint in perpetuity. It is made available under aCC-BY-NC-ND 4.0 International license.

Confocal Microscope System controlled by Nikon NIS-Elements software or a Zeiss 20×, 0.75 NA or 63×, 1.4 NA Plan Apo objective on a Zeiss LSM 880 system controlled by Zeiss ZEN software. Immunostained tissue culture cells were imaged using a Nikon 40×, 1.25 NA, Plan Apo, silicone-immersion objective on a Nikon spinning disk confocal system equipped with a Yokogawa CSU-X1 unit and a Prime 95B sCMOS camera (Photometrics) controlled by Nikon NIS-Elements software.

Protein labeling

Human plasma fibronectin was purified as previously described (*36*). For fibronectin labeling, NHS-Atto647N (ATTO-TEC, AD 647N-31) was dissolved in DMSO to 10 mM and stored in a desiccated container at -20°C as 10 µL aliquots. Labeling buffer was 20 parts PBS with 1 part 0.2 M $NaHCO_3$ (pH 9.0), which was adjusted to pH 8.3. For labeling, 1 mL fibronectin was exchanged to the labeling buffer using a spin desalting column (Thermo Fisher, 89891). The fibronectin concentration after buffer exchange was determined by absorbance at 280 nm (2.3 mg/mL), which was used to calculate the amount of NHS-Atto647N equivalent to 4× times molar excess of fibronectin (3.4 µL). The labeling mix was incubated for 45 min at room temperature, then unlabeled dye was removed by buffer exchange into PBS using a spin desalting column. Insoluble Atto647N-fibronectin was removed by centrifugation at 13,000× rpm for 30 min at 4°C. The concentration of cleared Atto647N-fibronectin and the degree of labeling (DOL) were calculated from absorbance at 280 nm and 646 nm with a dye-specific correction factor 0.03 (using the Atto calculation formula; 0.84 mg/mL, DOL 1.7). Atto647N-fibronectin was then aliquoted and stored at -80°C. A similar procedure was used to label collagen IV antibody (MilliporeSigma, AB769) with NHS-AF680 (Thermo Fisher, A20008), but a 50 mM borate buffer (pH 9.0) was used as the labeling buffer and labeled antibodies were stored in PBS at 4°C.

Image processing and analysis

All images acquired on the Nikon A1R Confocal System were denoised using the Denoise.ai function of the Nikon NIS-Elements software. All other image processing was performed in Fiji (*37*), an ImageJ distribution. Customized Python, Jython and ImageJ Macro scripts were used for automating or facilitating image analysis and data visualization in this study (see Data and materials availability). Automatic 3D cell tracking and surface rendering were performed using Imaris 9.5.0 (Bitplane). Manual curation of semi-automatic cell tracking was performed in Fiji using the TrackMate (*38*) plugin. Manual surface reconstruction (used in **Fig. S3D** and **Movie S7**) was performed by drawing polylines along the epithelial surface at sparse z planes (~6 µm intervals) on x-y view and resliced y-z view image stacks in Fiji, which were used for interpolation and plotting using customized Python scripts. For automated cell counting in the attachment assay, nuclear fluorescence images were smoothed by Gaussian filter (sigma = 2 pixels), contrast enhanced by the MorphoLibJ (*39*) white top hat filter (disk, radius = 10), thresholded and counted using the Analyze Particles function of ImageJ. For manual bud counting, several efforts were made to minimize bias. First, file names of all images were scrambled before counting for observer blinding. Second, the same investigator performed the counting of all spheroids (K.M.) or all salivary glands (S.W.) to avoid between-person variance. Third, an explicit criterion was used such that a bud was counted only when its protruding edge occupied at least one third of a circle.

Data and materials availability

Data for reproducing all plots in this study are available in Figshare with the identifier [10.35092/yhjc.12145626 (reserved DOI); private link for peer review only: https://figshare.com/s/4d9ec0683d9f6d4ef951]. Raw data that support the findings of this study

bioRxiv preprint doi: https://doi.org/10.1101/2020.06.24.165795; this version posted June 24, 2020. The copyright holder for this preprint (which was not certified by peer review) is the author/funder, who has granted bioRxiv a license to display the preprint in perpetuity. It is made available under aCC-BY-NC-ND 4.0 International license.

and biological materials such as plasmids, cell lines and mice are available from the corresponding author upon reasonable request. Customized scripts and usage instructions are available from Github: https://github.com/snownontrace/public-scripts-Wang2020-branching-morphogenesis .

bioRxiv preprint doi: https://doi.org/10.1101/2020.06.24.165795; this version posted June 24, 2020. The copyright holder for this preprint (which was not certified by peer review) is the author/funder, who has granted bioRxiv a license to display the preprint in perpetuity. It is made available under aCC-BY-NC-ND 4.0 International license.

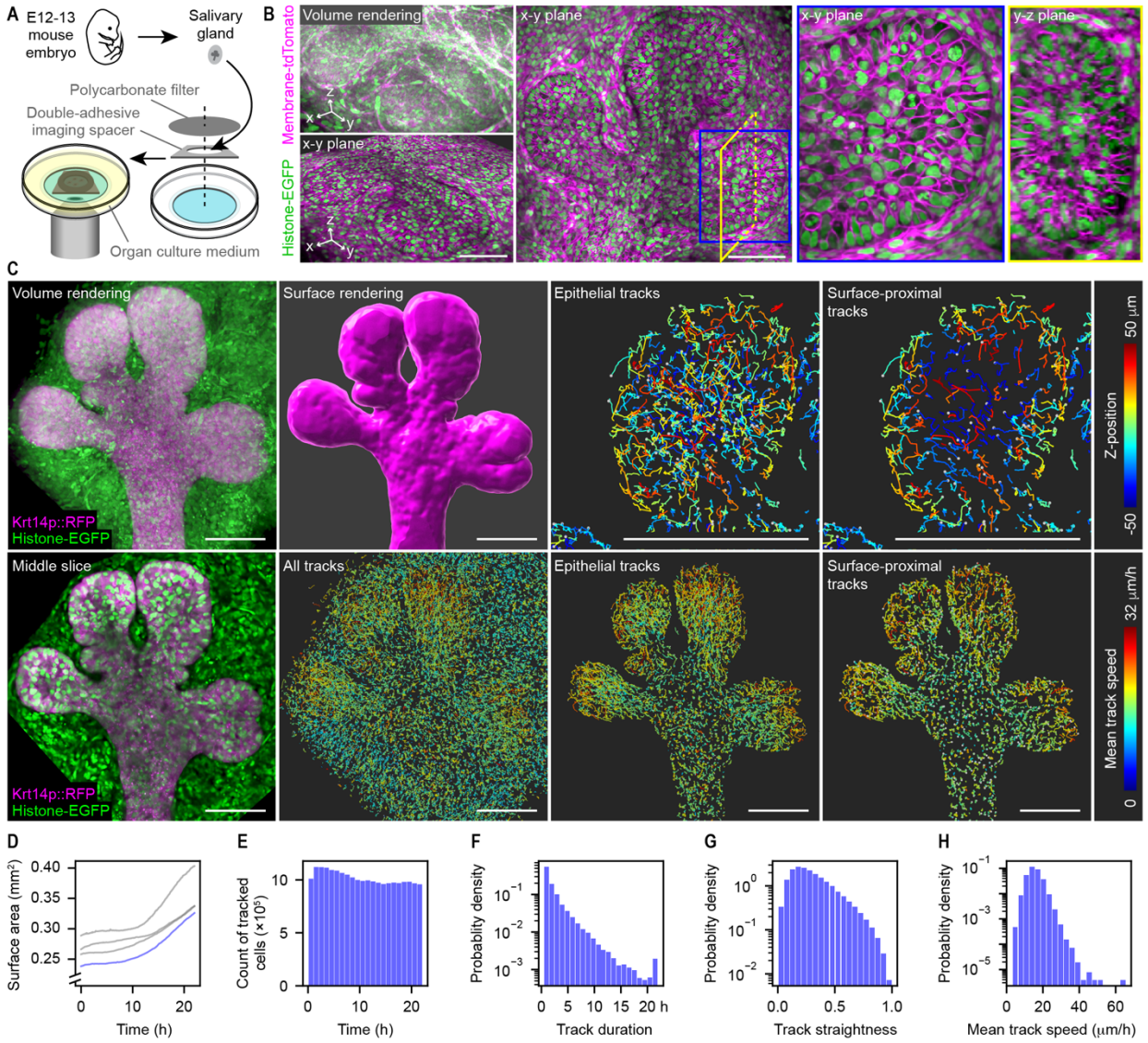

Fig. S1.

Imaging and cell tracking of mouse embryonic salivary glands. (**A**) Schematic describing sample preparation for live imaging of wholemount mouse embryonic salivary glands. (**B**) Different views of a volumetric imaging data set at the first time point. (**C**) Views of images, surface rendering and cell tracks of another volumetric imaging data set. (**D**) Plot of total epithelial surface area over time of 4 imaging data sets. The blue line is from the data set shown in (C). (**E**) Histogram of the number of tracked cells over time for the data set shown in (C). (**F** to **H**) Distribution plots of the track duration, track straightness and mean track speed (average over its duration) for the data set shown in (C). Note that the y-axis is in log-scale to facilitate visualization of small numbers. Scale bars, 100 µm.

bioRxiv preprint doi: https://doi.org/10.1101/2020.06.24.165795; this version posted June 24, 2020. The copyright holder for this preprint (which was not certified by peer review) is the author/funder, who has granted bioRxiv a license to display the preprint in perpetuity. It is made available under aCC-BY-NC-ND 4.0 International license.

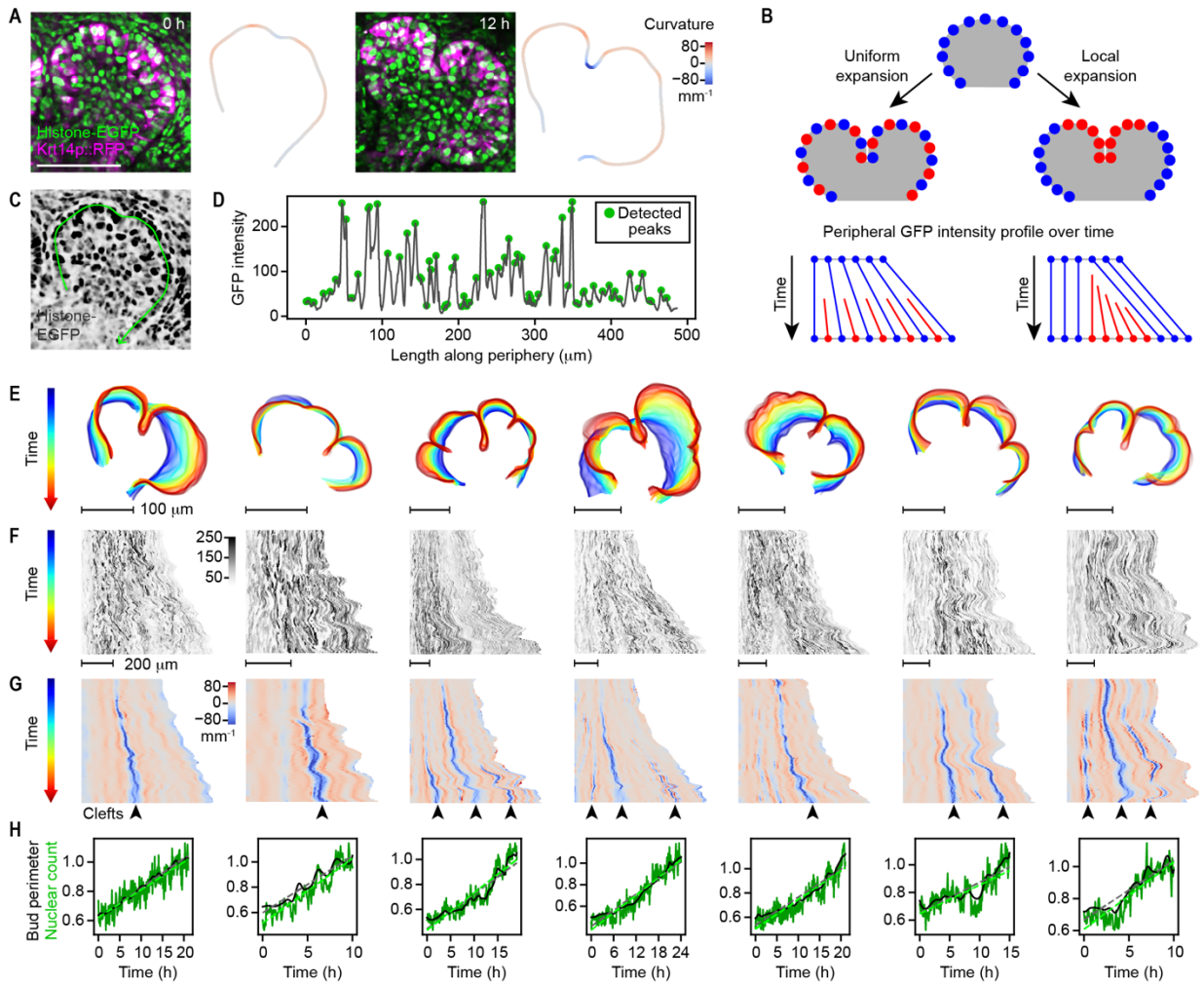

Fig. S2.

Uniform expansion of the surface epithelial layer during salivary gland clefting. (**A**) Two-photon microscopy images and epithelial surface outline color-coded by local curvature of an E13 transgenic mouse salivary gland. Scale bar, 100 μm. (**B**) Schematics of uniform vs. local expansion of the epithelial surface and their predicted peripheral GFP intensity profile over time. (**C**) Inverted histone-EGFP image from the same image in (A) at 0 h. The green curved line indicates the positions where peripheral GFP intensities were sampled. (**D**) Plot of GFP intensity along the green curve in (C). Green dots indicate automatically detected peaks used to quantify nuclear counts. (**E** to **H**) Outlines of the epithelial surface at the middle slice (E), heatmaps of the peripheral GFP intensity (F) and curvature (G), and plots of the bud perimeter (H; black) and peripheral nuclear count (H; green) over time. Dashed lines in (H) indicate fitted linear models.

bioRxiv preprint doi: https://doi.org/10.1101/2020.06.24.165795; this version posted June 24, 2020. The copyright holder for this preprint (which was not certified by peer review) is the author/funder, who has granted bioRxiv a license to display the preprint in perpetuity. It is made available under aCC-BY-NC-ND 4.0 International license.

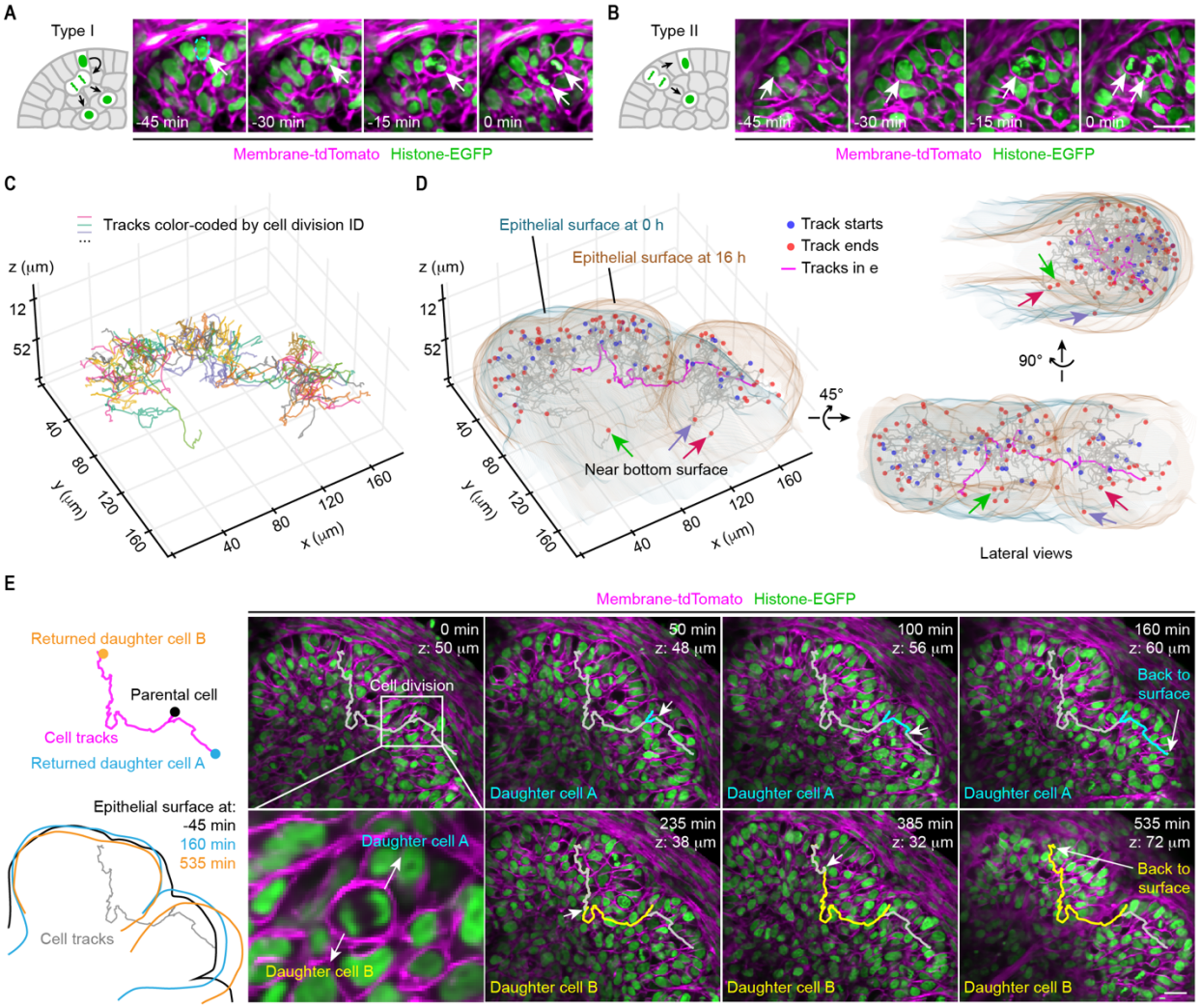

Fig. S3.

Robust surface return of interior daughter cells after cell division of surface epithelial cells. (**A** and **B**) Schematics and two-photon microscopy image sequences showing the two observed types of surface cell division. The 0 min images are the same as those in Fig. 2A. (**C** and **D**) 3D plots of cell tracks following 42 surface cell divisions and the surface return of their daughter cells. (**E**) Schematics (left) and snapshots of time-lapse two-photon images (right) following a cell division and tracks of both daughter cells highlighted in (D) and (E). White arrows point to tracked cells. Scale bars, 20 μm.

bioRxiv preprint doi: https://doi.org/10.1101/2020.06.24.165795; this version posted June 24, 2020. The copyright holder for this preprint (which was not certified by peer review) is the author/funder, who has granted bioRxiv a license to display the preprint in perpetuity. It is made available under aCC-BY-NC-ND 4.0 International license.

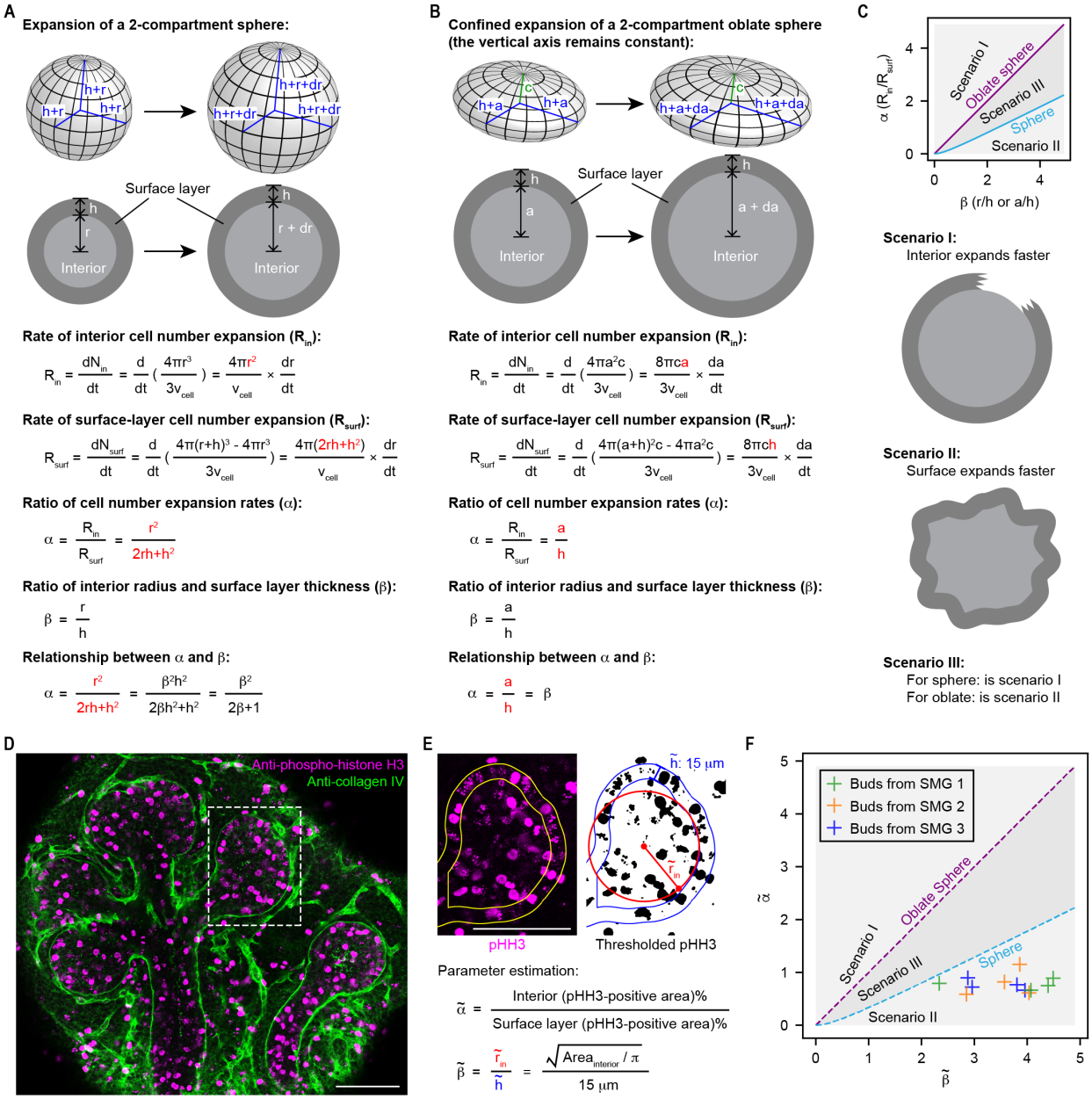

Fig. S4.

A simplified numerical model of stratified epithelial branching. (**A** and **B**) Schematics and mathematical derivation of the relationship between the parameters α and β during the expansion of a 2-compartment sphere (A) or an oblate sphere (B). Here α is the ratio of cell number expansion rates (interior vs. surface layer), whereas β is the ratio of interior radius vs. surface layer thickness. Important assumptions include: 1. Average cell volume remains constant. 2. Surface layer thickness remains constant. 3. The sphere or oblate sphere is filled with cells without spaces between cells. 4. The surface layer and interior compartments do not intermix. (**C**) Top: plot of α vs. β. In the case of a sphere or an oblate sphere, α and β must fall on the turquoise or the purple line. Bottom: illustrations of the three possible scenarios of parameter combination. (**D**) Confocal immunofluorescence image of an E13 salivary gland. Anti-phospho-histone H3 (pHH3) marks mitotic cells, and anti-collagen IV marks the basement membrane. (**E**) Top: images

bioRxiv preprint doi: https://doi.org/10.1101/2020.06.24.165795; this version posted June 24, 2020. The copyright holder for this preprint (which was not certified by peer review) is the author/funder, who has granted bioRxiv a license to display the preprint in perpetuity. It is made available under aCC-BY-NC-ND 4.0 International license.

illustrating the thresholding of the pHH3 signal. The outer boundary was automatically determined from anti-E-cadherin staining (not shown), which was shrunken by 15 μm to obtain the interior boundary. Bottom: equations showing how estimated α and β were determined. (**F**) Plot of estimated α and β pairs for 12 epithelial buds from 3 submandibular salivary glands (SMG). Note that all parameter pairs fall within the Scenario II domain. Scale bars, 100 μm.

bioRxiv preprint doi: https://doi.org/10.1101/2020.06.24.165795; this version posted June 24, 2020. The copyright holder for this preprint (which was not certified by peer review) is the author/funder, who has granted bioRxiv a license to display the preprint in perpetuity. It is made available under aCC-BY-NC-ND 4.0 International license.

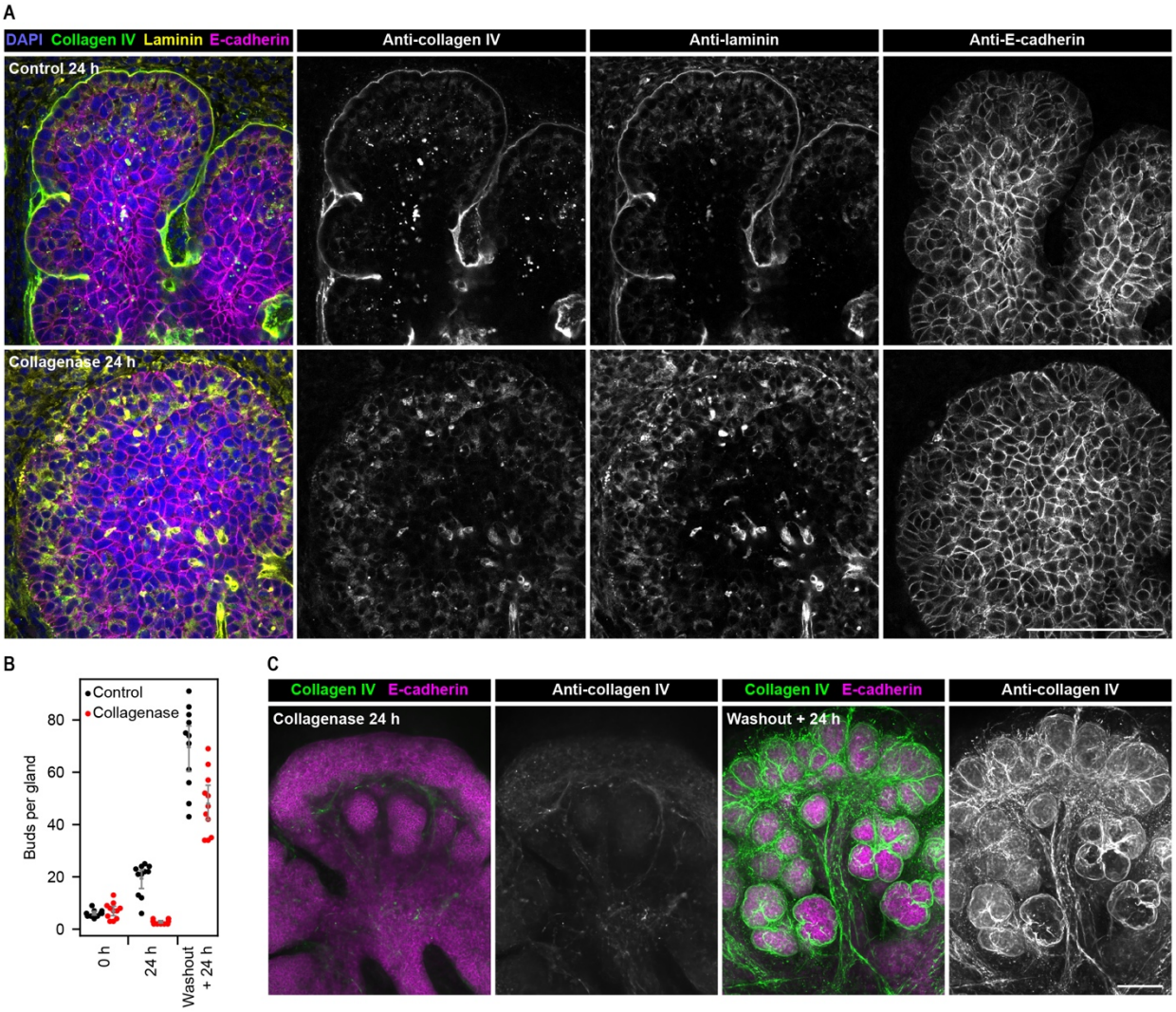

Fig. S5.

Accelerated branching of salivary glands upon basement membrane recovery from enzymatic disruption. (**A**) Confocal immunofluorescence images of control or collagenase treated glands at 24 h. (**B**) Plot of bud number per gland over time (the same data set in Fig. 2G). N=11 for each group. (**C**) Maximum intensity projection of the bottom 60 μm z-stack confocal immunofluorescence images of a collagenase-treated salivary gland at 24 h (left) or a collagenase treated gland at 24 h post washout (right). Scale bars, 100 μm.

bioRxiv preprint doi: https://doi.org/10.1101/2020.06.24.165795; this version posted June 24, 2020. The copyright holder for this preprint (which was not certified by peer review) is the author/funder, who has granted bioRxiv a license to display the preprint in perpetuity. It is made available under aCC-BY-NC-ND 4.0 International license.

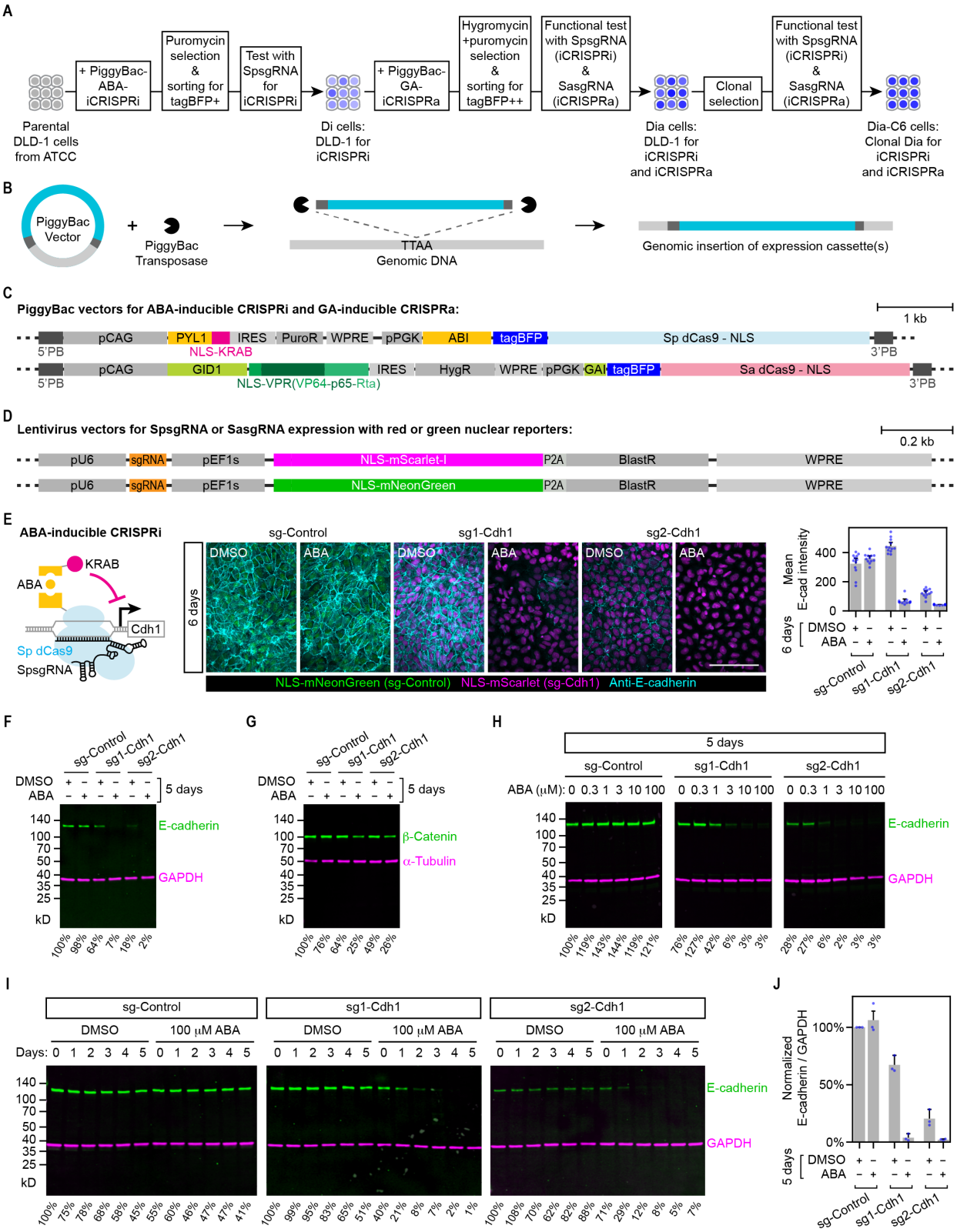

bioRxiv preprint doi: https://doi.org/10.1101/2020.06.24.165795; this version posted June 24, 2020. The copyright holder for this preprint (which was not certified by peer review) is the author/funder, who has granted bioRxiv a license to display the preprint in perpetuity. It is made available under aCC-BY-NC-ND 4.0 International license.

Fig. S6.

Establishing a clonal cell line for inducible modulation of cell adhesions. (**A**) Schematics illustrating engineering of a clonal Dia-C6 cell line from DLD-1. Dia cells stably express 4 transgenes that enable inducible transcriptional activation or repression. (**B**) Schematics of the PiggyBac transposon system used to introduce transgenes. (**C**) Schematics of 2 PiggyBac vectors expressing 4 transgenes for inducible transcriptional modulation. (**D**) Schematics of lentivirus vectors used to deliver guide RNAs for transcriptional modulation. (**E**) Left: schematic of the ABA-inducible transcriptional repression system. Middle: maximum intensity projection of confocal images of Dia cells expressing indicated sgRNAs. Scale bar, 100 μm. Green and magenta nuclei indicate cells expressing sgRNAs. Right: plot of mean E-cadherin intensities of indicated experimental conditions. N=12 fields of view for each group. (**F** to **I**) Western blots showing the expression level of E-cadherin or β-catenin under the indicated experimental conditions. Percentage levels under each lane are normalized ratios of E-cadherin to GAPDH or β-catenin to α-tubulin intensities of that lane. Normalizations in (F, G, H) are versus the control group (sg-Control, DMSO) from the same blot, whereas normalizations in (I) are versus the first lane (Day 0, DMSO) on the same blot. (**J**) Plot of normalized ratios of E-cadherin to GAPDH intensities of Dia cells expressing sg-Control, sg1-Cdh1 or sg2-Cdh1 treated with DMSO or ABA for 5 days. Normalizations are versus the control group (sg-Control, DMSO) for each of the 3 biological replicates. Error bars in (E, J) are 95% confidence intervals.

bioRxiv preprint doi: https://doi.org/10.1101/2020.06.24.165795; this version posted June 24, 2020. The copyright holder for this preprint (which was not certified by peer review) is the author/funder, who has granted bioRxiv a license to display the preprint in perpetuity. It is made available under aCC-BY-NC-ND 4.0 International license.

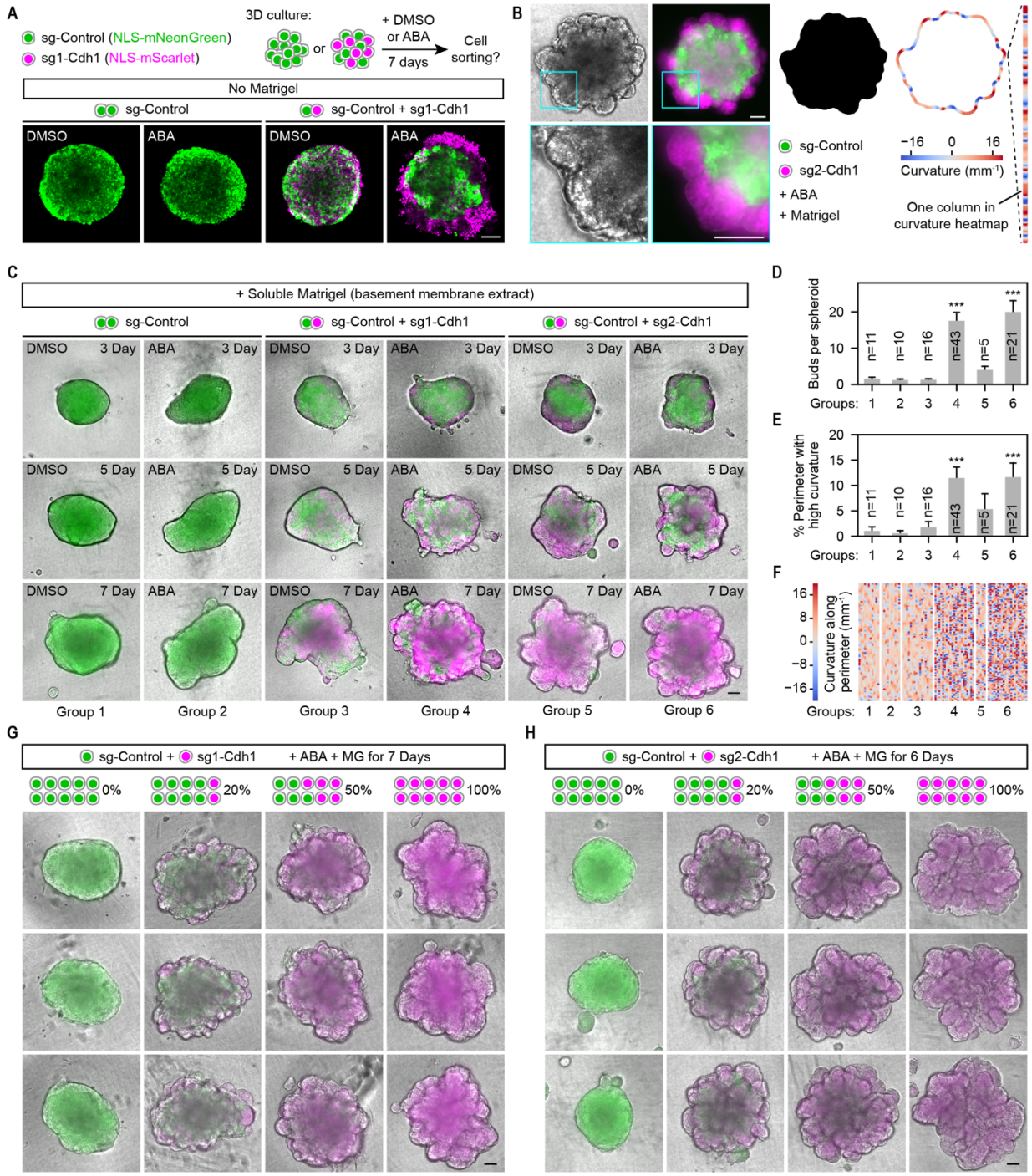

Fig. S7.

Reducing cell-cell adhesion and inducing basement membrane formation is sufficient to induce branching of a stratified epithelium. (**A**) Top: schematics of the experimental design. Bottom: confocal fluorescence images of spheroids for indicated experimental conditions. (**B**) Left: phase contrast and epifluorescence images of a spheroid. Right: binary mask image segmented from merged green and red fluorescence, and its boundary outline color-coded by the local curvature. Each column of curvature heatmaps represent a straightened outline color-coded by

bioRxiv preprint doi: https://doi.org/10.1101/2020.06.24.165795; this version posted June 24, 2020. The copyright holder for this preprint (which was not certified by peer review) is the author/funder, who has granted bioRxiv a license to display the preprint in perpetuity. It is made available under aCC-BY-NC-ND 4.0 International license.

curvature. (**C**) Merged phase contrast and epifluorescence images of spheroids from indicated experimental conditions at 3 time points. (**D** and **E**) Bar plots of bud number or percentage of high-curvature perimeter length (|curvature|>20 mm^{-1}). (**F**) Heatmap showing color-coded curvature along spheroid perimeters. Each column is one spheroid. Only 21 of 43 Group 4 samples were included in the heatmap to save space. (**G** and **H**) Merged phase contrast and epifluorescence images of spheroids from indicated experimental conditions with different mixing ratios of control and E-cadherin downregulated cells. Scale bars, 100 μm.

bioRxiv preprint doi: https://doi.org/10.1101/2020.06.24.165795; this version posted June 24, 2020. The copyright holder for this preprint (which was not certified by peer review) is the author/funder, who has granted bioRxiv a license to display the preprint in perpetuity. It is made available under aCC-BY-NC-ND 4.0 International license.

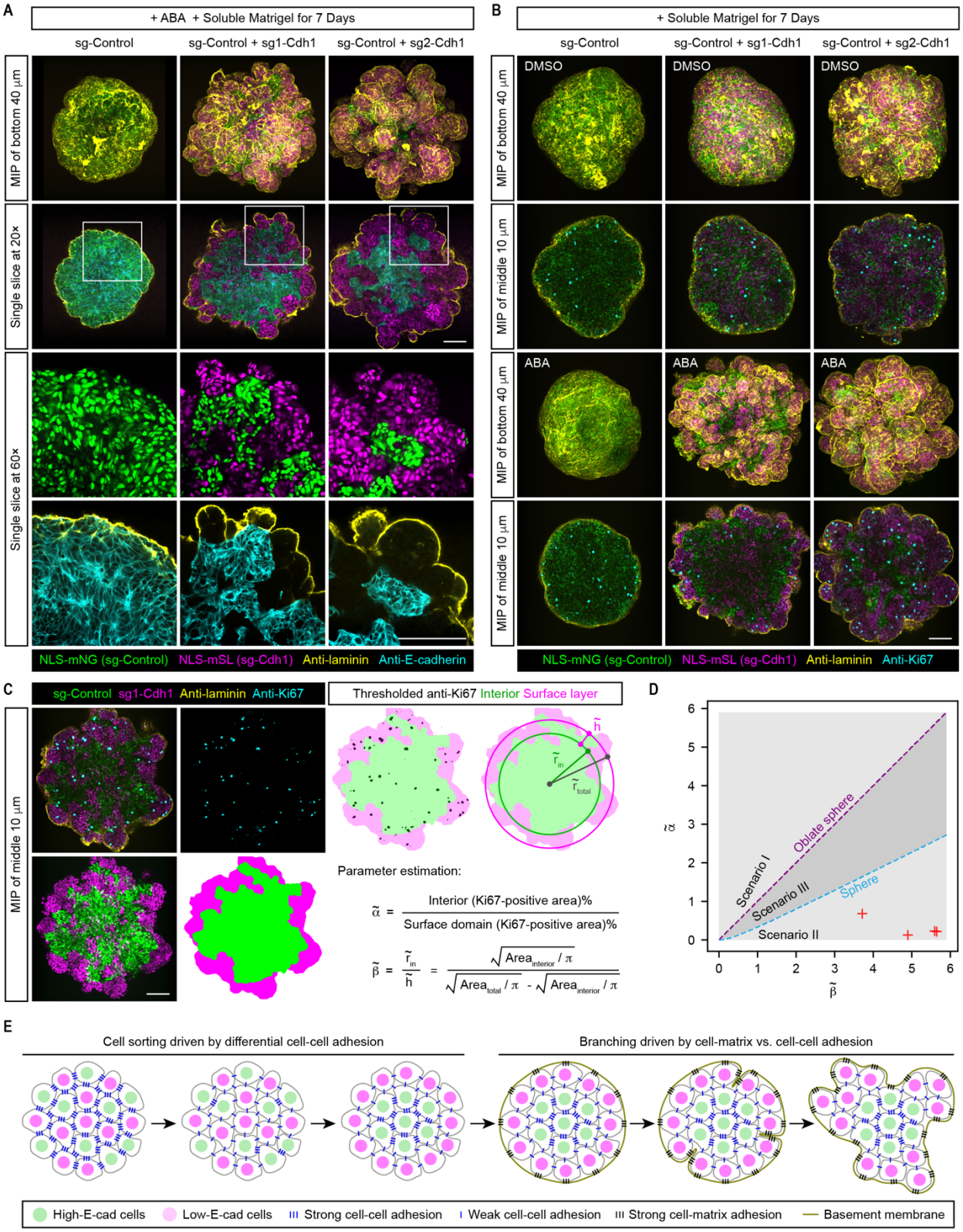

bioRxiv preprint doi: https://doi.org/10.1101/2020.06.24.165795; this version posted June 24, 2020. The copyright holder for this preprint (which was not certified by peer review) is the author/funder, who has granted bioRxiv a license to display the preprint in perpetuity. It is made available under aCC-BY-NC-ND 4.0 International license.

Fig. S8.

Cells with reduced E-cadherin expression in spheroids sort to the surface and proliferate faster than interior cells. (**A** and **B**) Confocal fluorescence images of spheroids from indicated experimental conditions immunostained with laminin (yellow; a basement membrane marker) and E-cadherin or Ki67 (cyan; a proliferation marker). MIP, maximum intensity projection. (**C**) Images, schematics and equations illustrating the thresholding of the Ki67 signal and the estimation of α and β parameters. (**D**) Plot of estimated α and β pairs for 4 spheroids with mixed sg-Control and sg1-Cdh1-expressing Dia cells. (**E**) Schematics illustrating the cell sorting and branching of a stratified epithelium with mixed populations of high vs. low E-cadherin-expressing cells. Scale bars, 100 μm.

bioRxiv preprint doi: https://doi.org/10.1101/2020.06.24.165795; this version posted June 24, 2020. The copyright holder for this preprint (which was not certified by peer review) is the author/funder, who has granted bioRxiv a license to display the preprint in perpetuity. It is made available under aCC-BY-NC-ND 4.0 International license.

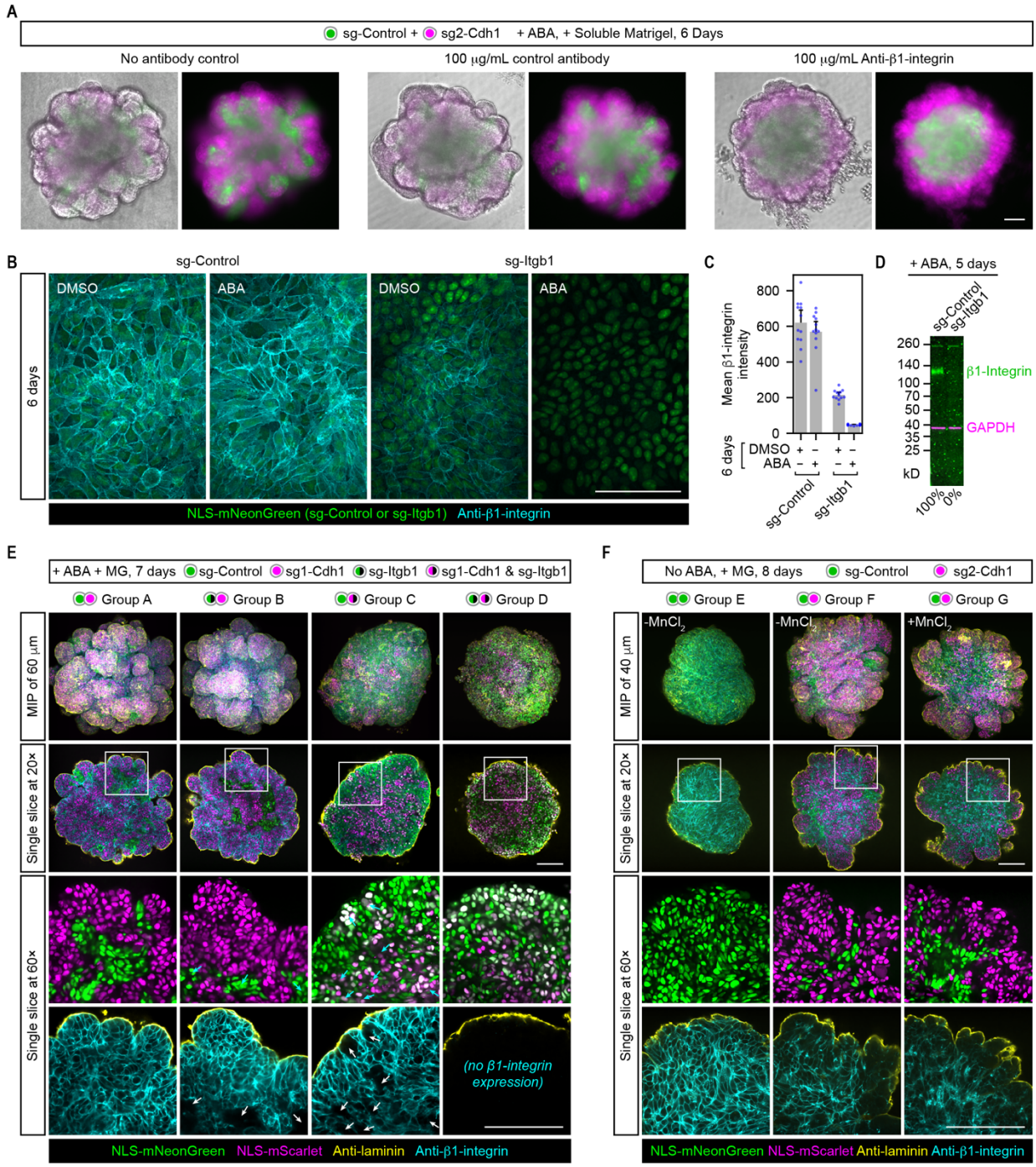

Fig. S9.

Reconstituted epithelial branching requires β1-integrin-mediated cell-matrix adhesion and can be promoted by elevating cell-matrix adhesion strength. (**A**) Merged phase contrast and epifluorescence images of spheroids from indicated experimental conditions. The α5-integrin antibody (clone mAb16) was used as a species-matched control antibody for the β1-integrin blocking antibody (clone mAb13). N=6 from 2 independent experiments. (**B**) Maximum intensity projection of confocal immunofluorescence images of 2D-cultured Dia cells expressing indicated sgRNAs. Green nuclei indicate cells expressing the sgRNAs. (**C**) Plot of mean β1-integrin

bioRxiv preprint doi: https://doi.org/10.1101/2020.06.24.165795; this version posted June 24, 2020. The copyright holder for this preprint (which was not certified by peer review) is the author/funder, who has granted bioRxiv a license to display the preprint in perpetuity. It is made available under aCC-BY-NC-ND 4.0 International license.

intensities under the indicated experimental conditions. N=12 fields of view for each group. (**D**) Western blot showing expression levels of β1-integrin under indicated experimental conditions. Percentage levels under each lane are normalized ratios of β1-integrin to GAPDH intensities of that lane. (**E** and **F**) Confocal fluorescence images of spheroids under indicated experimental conditions immunostained with laminin (yellow; a basement membrane marker) and β1-integrin (cyan). Note that green nuclei in (E) indicate either sg-Control or sg-Itgb1 expression depending on the experimental group. Arrows point to clusters of cells that lost their β1-integrin expression. MIP, maximum intensity projection. Scale bars, 100 μm.

bioRxiv preprint doi: https://doi.org/10.1101/2020.06.24.165795; this version posted June 24, 2020. The copyright holder for this preprint (which was not certified by peer review) is the author/funder, who has granted bioRxiv a license to display the preprint in perpetuity. It is made available under aCC-BY-NC-ND 4.0 International license.

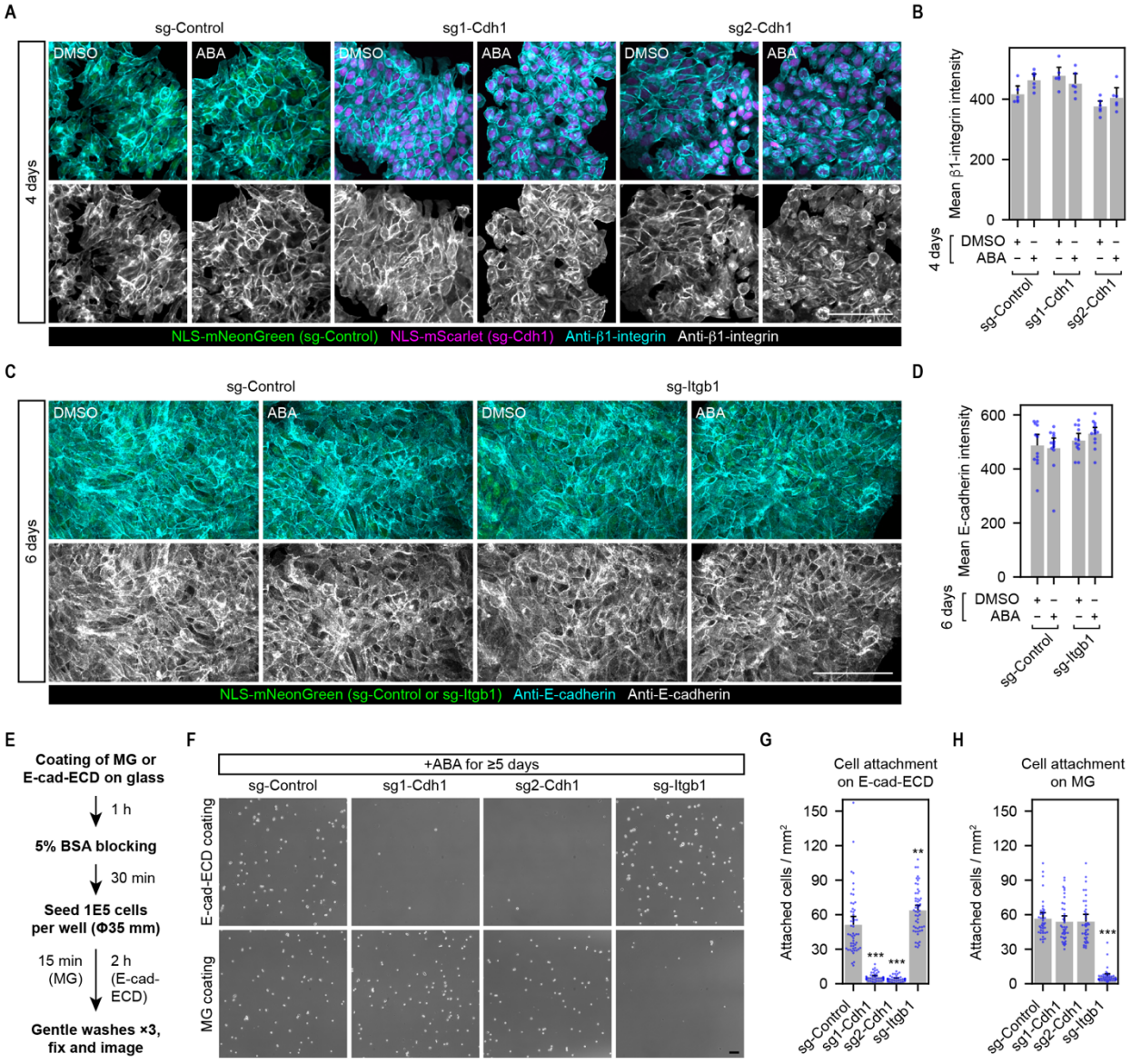

Fig. S10.

Reducing E-cadherin or β1-integrin expression inhibits cell attachment to E-cadherin extracellular domain or Matrigel-coated surfaces, respectively. (**A** and **C**) Maximum intensity projection of confocal immunofluorescence images of 2D-cultured cells. Green or magenta nuclei indicate cells expressing the indicated sgRNAs. (**B** and **D**) Plots of mean β1-integrin or E-cadherin intensities under the indicated experimental conditions. N=6 (B) or 12 (D) fields of view for each group. (**E**) Schematics illustrating experimental procedures for the cell attachment assays. MG, Matrigel; E-cad-ECD, E-cadherin extracellular domain. (**F**) Phase contrast images of attached cells under indicated experimental conditions. (**G** and **H**) Plots of attached cells under indicated experimental conditions. N=52, 39, 39, 52 fields of view for groups in (G). N=39 fields of view for each group in (H). Each experimental group had 3 or 4 biological replicates, and each had 13 fields of view. The full set of experiments was done twice. Scale bars, 100 μm.

bioRxiv preprint doi: https://doi.org/10.1101/2020.06.24.165795; this version posted June 24, 2020. The copyright holder for this preprint (which was not certified by peer review) is the author/funder, who has granted bioRxiv a license to display the preprint in perpetuity. It is made available under aCC-BY-NC-ND 4.0 International license.

Movie Legends:

Movie S1.

Volumetric time-lapse movie of a branching embryonic salivary gland. Salivary gland from a 13-day transgenic mouse embryo expressing membrane-tdTomato and histone-EGFP. Time-lapse volumetric two-photon microscopy images were acquired at 2-μm z steps over a 100 μm z range at 5-minute intervals for 20 hours. The first half of the movie shows different views of the imaging volume at the first time point. The second half of the movie shows time-lapse sequences of the middle x-y plane (left) or 3D rendering of the middle 40 μm-thick volume of a branching epithelial bud (right).

Movie S2.

3D cell migration tracks from a volumetric time-lapse imaging data set of a branching salivary gland. Salivary gland from a 13-day transgenic mouse embryo expressing membrane-tdTomato and histone-EGFP. Tracks shown at each time point represent cell migration trajectories of the previous 4 hours. Tracks are color coded by mean track speed (left) or track straightness (right).

Movie S3.

Dynamics of surface-layer epithelial cells highlighted by KikGR photoconversion. Salivary gland from a 13-day transgenic mouse embryo expressing the photoconvertible fluorescent protein KikGR. Native KikGR has green fluorescence, which converts to red fluorescence after blue light excitation. Magenta color indicates photoconverted KikGR.

Movie S4.

Volumetric time-lapse movie of a branching salivary gland (left) and 3D rendering of the epithelial surface (right). Salivary gland from a 13-day transgenic mouse embryo expressing histone-EGFP and a homozygous epithelial RFP reporter driven by the Krt14 promoter (Krt14p::RFP). The 3D rendering of the epithelial surface is based on the Krt14p::RFP reporter.

Movie S5.

Surface-proximal 3D cell migration tracks from the same data set shown in Movie S4. Movies show only epithelial cell tracks for which the closest distance to the gland surface was ≤ 15 μm. White dots indicate cell centroids, and the tracks shown at each time point represent cell migration trajectories spanning the previous 2 hours. Tracks are color coded by mean track speed (left) or the z position (right).

Movie S6.

Different views of a branching epithelial bud from a developing salivary gland. Salivary gland from a 13-day transgenic mouse embryo expressing histone-EGFP and a heterozygous epithelial RFP reporter driven by the Krt14 promoter (Krt14p::RFP). Note that the surface-layer epithelial cells expressing high RFP comprise a cell sheet that folds inward during clefting.

Movie S7.

3D tracking of daughter cells from surface-derived cell divisions. This movie has 3 sequential parts. The first part shows rotating views of 3D tracking plots of 84 daughter cells from 42 cell divisions relative to the epithelial surface. The second part shows “tracked cell highlighted” (left) and “tracked cell centered” (right) styles of a tracking example. The third part shows tracking of 16 pairs of daughter cells in the “tracked cell centered” style. Tracked cell is marked by a white

bioRxiv preprint doi: https://doi.org/10.1101/2020.06.24.165795; this version posted June 24, 2020. The copyright holder for this preprint (which was not certified by peer review) is the author/funder, who has granted bioRxiv a license to display the preprint in perpetuity. It is made available under aCC-BY-NC-ND 4.0 International license.

dot. Distance indicated is from the coverslip. Time indicates minutes from the onset of anaphase (0 min).

Movie S8.

Time-lapse movies of 3D spheroid cultures of engineered DLD-1 cells under indicated experimental conditions. Images are merged phase contrast and epifluorescence channels. Green and magenta indicate cells expressing sg-Control or sg-Cdh1, respectively. Abscisic acid (ABA) is a dimerizer used to induce robust transcriptional repression in engineered DLD-1 cells. DMSO is the vehicle control. Live imaging started 5 days post Matrigel and ABA or DMSO treatment.

Movie S9.

Time-lapse movies of a branching spheroid culture of engineered DLD-1 cells. Images in the main window are maximum intensity projections of confocal fluorescence images, and images in the upper left inset are single-slice confocal fluorescence images. Green and magenta indicate cells expressing sg-Control or sg2-Cdh1, respectively. Yellow indicates the basement membrane marked by Atto-647N labeled fibronectin. Arrows and arrowheads indicate forming clefts. Live imaging started 4 days post Matrigel and ABA treatment.